Energy & Buildings 373 (2026) 118361

Contents lists available at ScienceDirect

Energy & Buildings

journal homepage: www.elsevier.com/locate/enb

Modeling global vertical solar illuminance on building façades using adaptive neuro-fuzzy inference systems under all-sky conditions☆

M.I. Dieste-Velasco

Electromechanical Engineering Department, University of Burgos, Avda. de Cantabria s/n, Burgos, Spain

ARTICLE INFO

Keywords:
Global vertical illuminance
Façade daylighting performance
Daylight availability
Solar irradiance
Radiometric modeling
Building façades
ANFIS

ABSTRACT

Global vertical illuminance on building façades is used in daylighting analysis, façade performance assessment, and energy-efficient building design. However, direct measurements are rarely available at conventional meteorological stations, limiting assessments involving different orientations, sky conditions, and interannual variability. This study develops an ANFIS-based methodology to estimate global vertical illuminance for the four cardinal orientations (north, east, south, and west) using only commonly available radiometric and geometric variables: direct normal irradiance (DNI), diffuse horizontal irradiance (DHI), and the cosine of the incidence angle on each façade. Models were trained using 115,250 records from 2024 and evaluated using 750,294 records across six independent years (2019–2023 and 2025) to assess temporal robustness. Results show that the models adequately reproduce global vertical illuminance for all façades under all-sky conditions. Over the six independent years, normalized root mean square error (nRMSE) ranged from 9.91% to 22.60%, and normalized mean absolute error (nMAE) ranged from 6.44% to 15.83%. The largest errors occurred for the north-facing façade, whereas the east-, south-, and west-facing façades maintained nRMSE values of 16.50% or lower. The methodological contribution lies in directly estimating LGV from commonly available radiometric variables and façade incidence geometry, without requiring vertical irradiance measurements, explicit sky classification, or intermediate luminous-efficacy calculations. These results support the use of the proposed approach to estimate LGV at the study site when direct vertical measurements are unavailable. Transferability to other locations should be assessed through independent validation.

1. Introduction

Reliable information on illuminance incident on building façades is used to characterize outdoor daylight availability and evaluate building daylighting and energy performance under variable environmental conditions [1–3]. The resulting indoor daylight contribution depends on façade orientation and design, including window systems [4–6], and influences artificial lighting and shading control strategies, visual comfort, and glare risk [7]. In addition, the solar exposure of façade surfaces is relevant for assessing building-integrated photovoltaic potential, whose performance is strongly affected by building orientation, urban density, and shading conditions [8]. External vertical illuminance is also used as a metric for assessing daylight availability in dense urban configurations [9,10]. However, illuminance is rarely measured at conventional meteorological stations, which generally record radiometric variables instead [11]. Consequently, the analysis of global vertical illuminance (LGV) across different façade orientations, sky conditions, and extended periods often requires estimation models.

Solar irradiance on horizontal and tilted surfaces has been widely modeled [12], and most methods for deriving daylight illuminance from radiometric measurements rely on luminous efficacy, which relates illuminance to irradiance [3]. Research has focused primarily on horizontal surfaces, for which global, direct, and diffuse luminous efficacy models have been developed using local measurements, satellite data, atmospheric variables, and sky classifications [13–16]. However, fewer studies have addressed vertical surfaces [11,17–20]. Li et al. [17] analyzed diffuse luminous efficacy under the 15 CIE standard skies and extended the approach to vertical surfaces, showing that illuminance estimation improved when measured vertical solar irradiance was available. Aghimien and Li [18] developed a vertical luminous efficacy model based on measured solar irradiance, horizontal luminous efficacy, and sky luminance distributions, obtaining monthly normalized root mean square error (nRMSE) values ranging from 10.6% to 39.9%, depending on the month and façade orientation. A simplified method for estimating mean hourly diffuse illuminance on vertical surfaces was

☆ This article is part of a Special issue entitled: 'ENB_Extreme Climate Designs' published in Energy & Buildings.

E-mail address: midieste@ubu.es.

https://doi.org/10.1016/j.enbuild.2026.118361
Received 9 May 2026; Received in revised form 14 September 2026; Accepted 5 October 2026
Available online 6 October 2026
0378-7788/© 2026 The Author. Published by Elsevier B.V. This is an open access article under the CC BY-NC-ND license (http://creativecommons.org/licenses/by-nc-nd/4.0/).

Nomenclature

BHI	beam horizontal irradiance (W/m^2)
cos(θ)	cosine of the incidence angle on the façade
D	diffuse fraction
DHI	diffuse horizontal irradiance (W/m^2)
DNI	direct normal irradiance (W/m^2)
GHI	global horizontal irradiance (W/m^2)
d_n	day of the year
E_0	eccentricity correction factor of the Earth's orbit
Kt	clearness index
LGV	global vertical illuminance (lux)
LGV_E	global vertical illuminance measured on the east-facing façade (lux)
LGV_W	global vertical illuminance measured on the west-facing façade (lux)
LGV_S	global vertical illuminance measured on the south-facing façade (lux)
LGV_N	global vertical illuminance measured on the north-facing façade (lux)
m	relative optical air mass
RH	relative humidity (%)
T	air temperature (°C)
Z	solar zenith angle (rad)
α	solar altitude angle (rad)
Δ	sky brightness
ε	sky clearness

Statistical and goodness-of-fit variables

IA	Willmott's index of agreement
nMAE	normalized mean absolute error (%)
nMBE	normalized mean bias error (%)
nRMSE	normalized root mean square error (%)
R^2	coefficient of determination

Model variables

x_i	predictor variables
y	response variable
$\hat{y}$	predicted value
$\bar{y}$	mean value

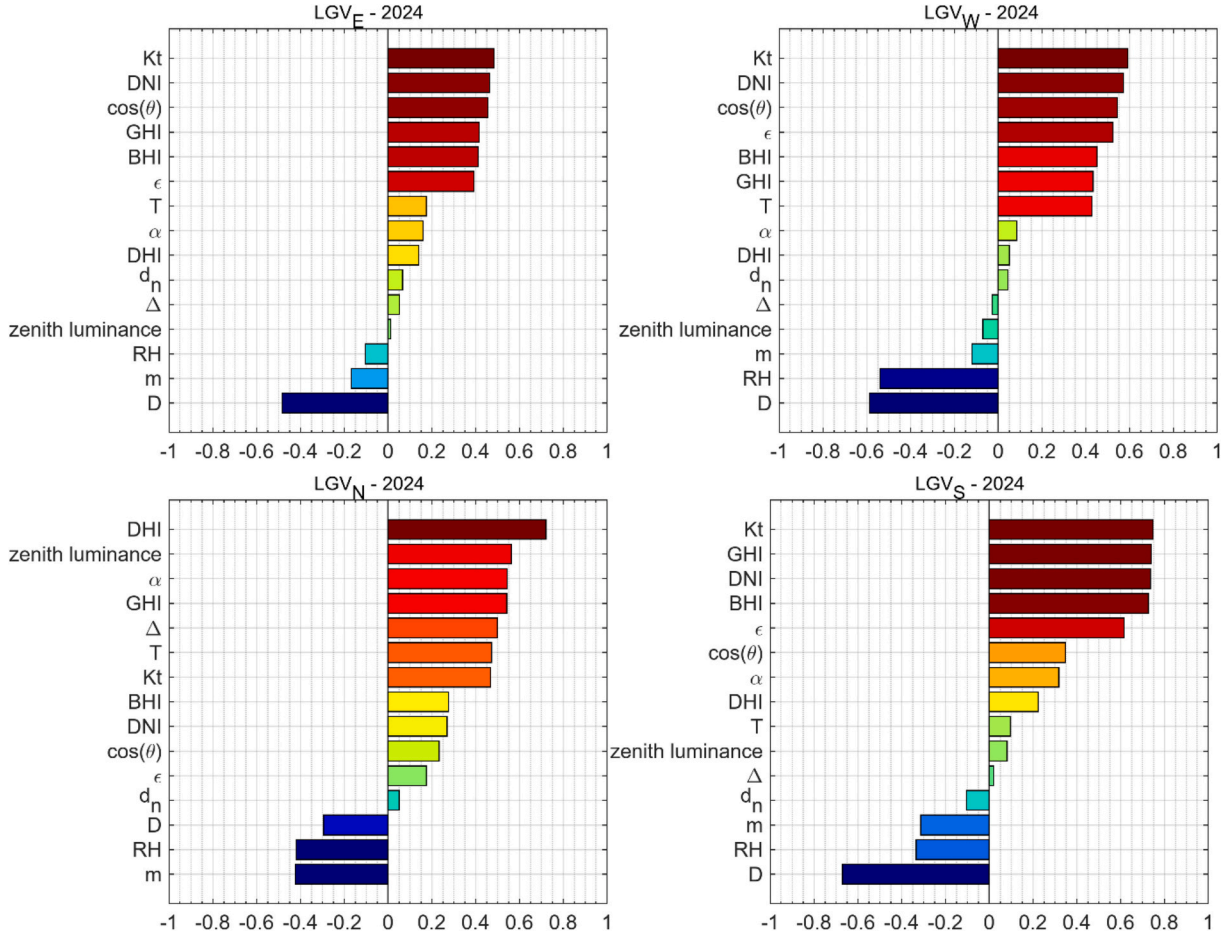


Fig. 1. Pearson correlation coefficients between the radiometric, atmospheric, and geometric variables and global vertical illuminance measured on the east-, west-, north-, and south-facing façades in the 2024 training dataset.

Table 1
Input configurations and model complexity for the compared methods.

Configuration	Predictors	ANFIS rules	ANFIS parameters	ANN hidden neurons	ANN parameters	Regression parameters
M1	DNI	4	12	4	13	3
M2	DNI, cos(θ)	16	32	8	33	6
M3	DNI, cos(θ), DHI	64	88	17	86	10

The results of the comparison among ANFIS, ANN, and regression are presented in the Results section.

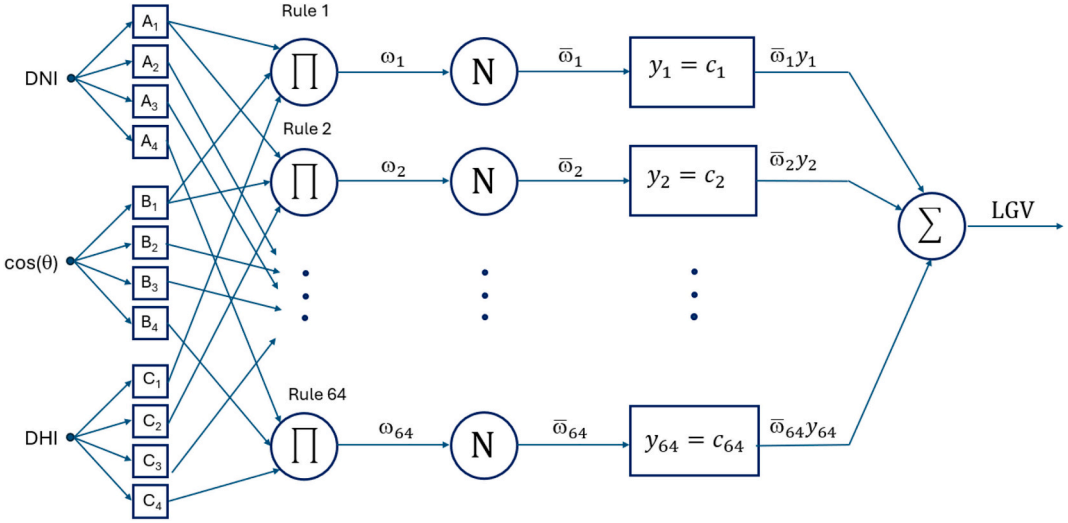


Fig. 2. Architecture of the zero-order Sugeno ANFIS used to estimate global vertical illuminance on the building façades.

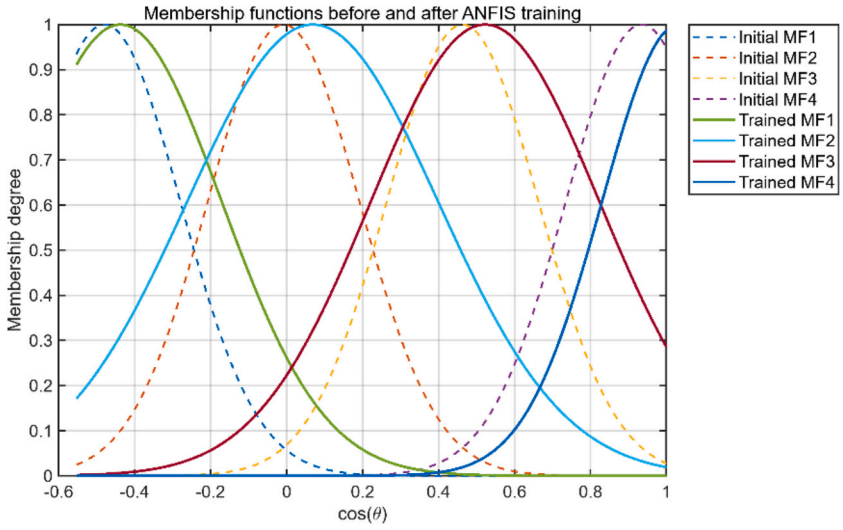


Fig. 3. Membership functions before and after ANFIS training for cos(θ) in the south orientation.

proposed in [19], although it required vertical diffuse irradiance and an orientation-specific constant luminous efficacy. Kong and Kim [20] used orientation-dependent regressions between vertical and horizontal illuminance ratios and obtained annual nRMSE values ranging from 15.97% to 24.79%. These studies demonstrate the feasibility of estimating vertical illuminance, but many of the proposed approaches require measured or modeled vertical irradiance, sky luminance distributions, prior sky classification, or locally calibrated relationships that may not be available at conventional radiometric stations.

Machine learning has also been applied to solar and lighting variables, although its use for directly estimating LGV remains limited. Neuro-fuzzy and fuzzy inference systems have been employed for adaptive lighting control, visual comfort assessment, and solar radiation prediction [21–23], while artificial neural networks have been used to estimate indoor illuminance distributions [24]. Li and Aghimien [25] developed vertical luminous efficacy models based on artificial neural networks and support vector machines, obtaining maximum percentage RMSE values below 20%. However, their final vertical illuminance estimates relied on measured vertical irradiance. Similarly, artificial neural networks were used in [26] to estimate global and diffuse luminous efficacy on horizontal surfaces under different sky conditions. Therefore, existing machine-learning studies either address different output variables or retain the luminous efficacy framework. Direct estimation of LGV from commonly available radiometric and geometric variables, without requiring measured vertical irradiance or an intermediate luminous efficacy calculation, remains insufficiently explored.

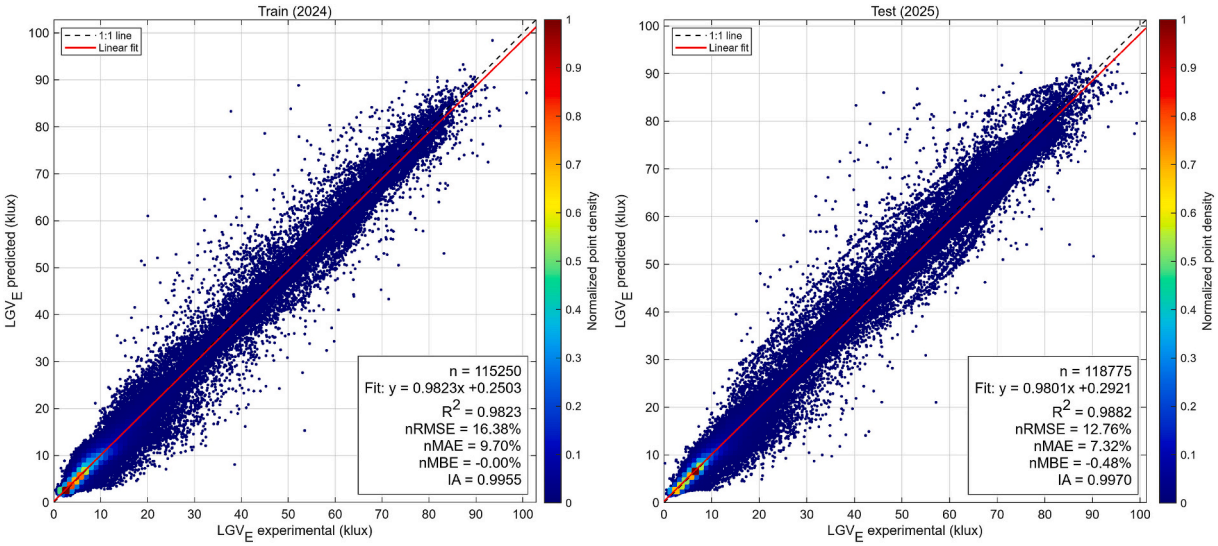


Fig. 4. Comparison between experimental and estimated LGV_E values for the training (2024) and testing (2025) datasets.

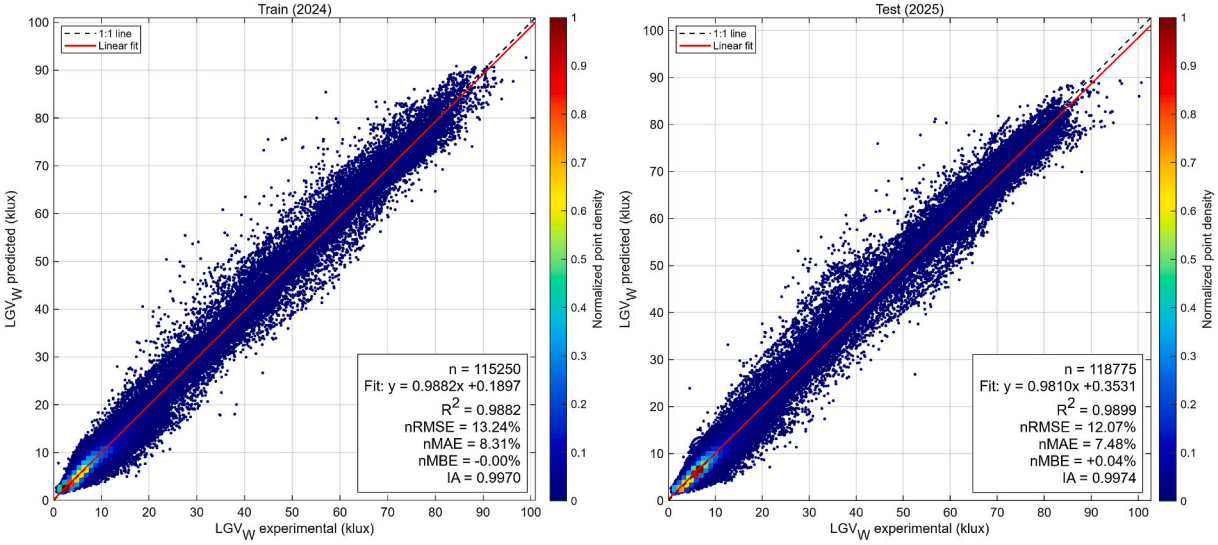


Fig. 5. Comparison between experimental and estimated LGV_W values for the training (2024) and testing (2025) datasets.

To address this gap, the present study develops four orientation-specific adaptive neuro-fuzzy inference system (ANFIS) models to estimate LGV on north-, east-, south-, and west-facing façades under all-sky conditions. Each model uses the same reduced set of three physically meaningful inputs: direct normal irradiance (DNI), diffuse horizontal irradiance (DHI), and the cosine of the incidence angle on the corresponding façade, cos(θ). Together, these variables represent direct and diffuse radiation availability and façade incidence geometry. The methodological contribution of this study lies in three aspects: the direct estimation of LGV without requiring measured vertical irradiance or an intermediate luminous efficacy calculation; the use of the same reduced and physically grounded input set for the four façade orientations under all-sky conditions; and an extensive temporal evaluation using six independent years that were not employed during model training. The models were trained using 115,250 records from 2024 and evaluated using 750,294 records from 2019 to 2023 and 2025. Their performance was also compared with reference models trained and evaluated using the same datasets. This evaluation assesses the temporal robustness of the proposed models at the study site, but does not establish their spatial transferability, which requires independent validation at other locations.

The remainder of the paper is organized as follows: Section 2 presents the experimental data used and the methodology followed; Section 3 presents the modeling of global vertical solar illuminance; Section 4 presents and discusses the results; and Section 5 presents the conclusions obtained in this study.

2. Experimental data and methods

This section describes the experimental data, predictor variables, and statistical methods used to develop the proposed illuminance models under all-sky conditions for the four cardinal façade orientations. For this purpose, Matlab™ and the Fuzzy Logic Toolbox for Matlab™ [27] were used.

2.1. Measurement facilities and predictor variables used in the global vertical illuminance models

Vertical illuminance, as well as horizontal irradiance and atmospheric measurements gathered at the Vaulx-en-Velin (France) International Daylight Measurement Programme (IDMP) station (45°46′43″ N, 4°55′21″ E), were used in this study. Data collected in 2024 were used

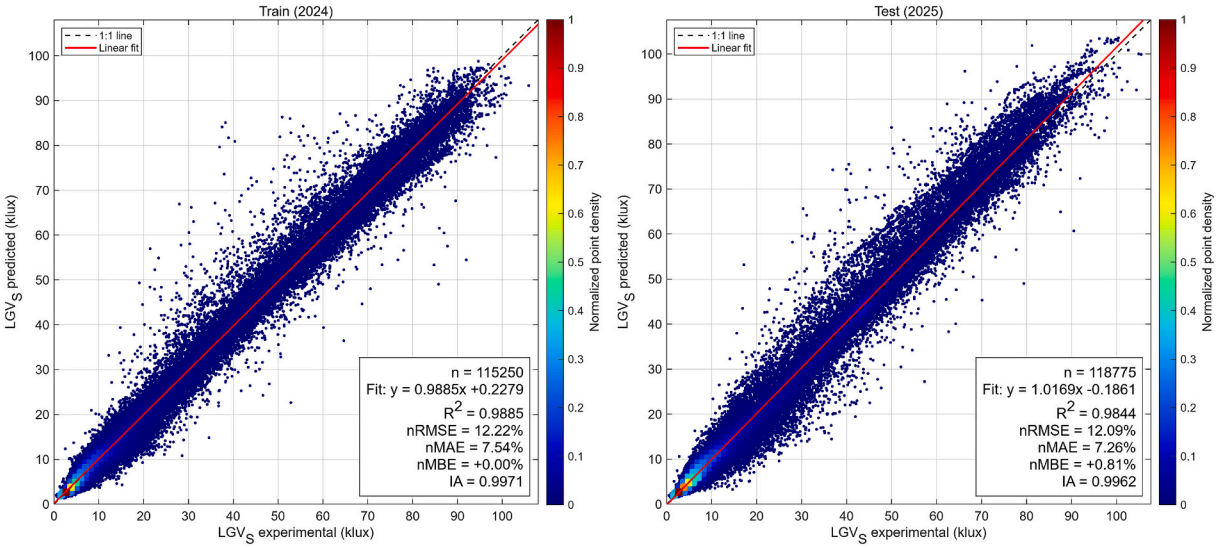


Fig. 6. Comparison between experimental and estimated LGV_S values for the training (2024) and testing (2025) datasets.

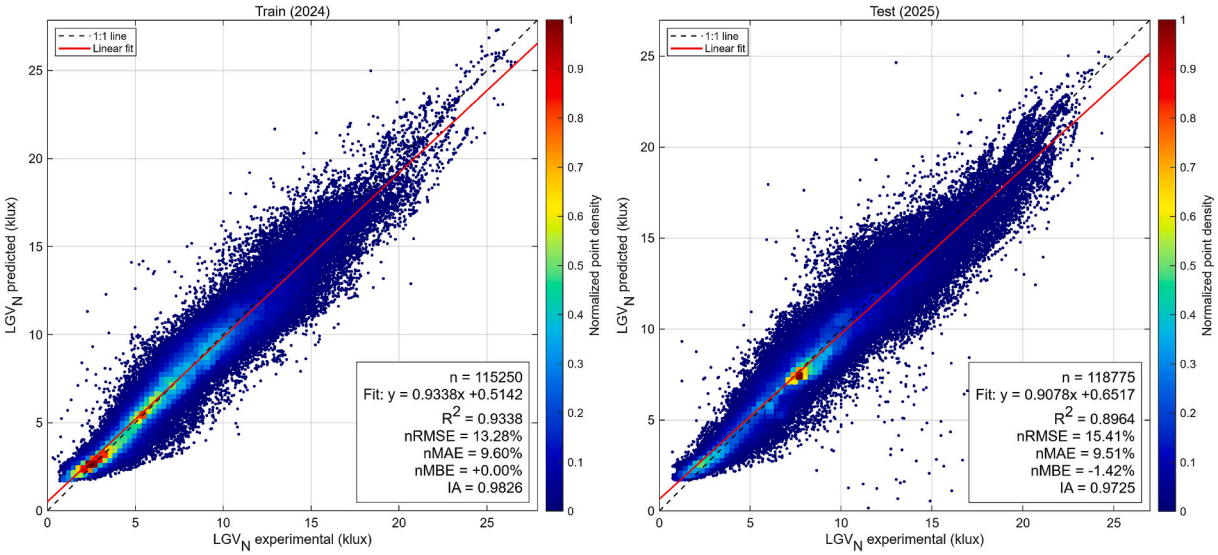


Fig. 7. Comparison between experimental and estimated LGV_N values for the training (2024) and testing (2025) datasets.

Table 2
Comparison of error metrics between M2 (DNI and cos(θ)) and M3 (DNI, cos(θ), and DHI) for the combined six-year independent evaluation dataset (750,294 records).

Orientation	nRMSE M2	nRMSE M3	nRMSE Relative reduction	nMAE M2	nMAE M3	nMAE Relative reduction
East	26.82%	14.39%	46.4%	19.14%	8.33%	56.5%
West	24.01%	12.17%	49.3%	17.74%	7.57%	57.3%
North	41.02%	16.60%	59.5%	32.74%	11.57%	64.7%
South	23.72%	11.16%	53.0%	17.73%	7.09%	60.0%

for model training, whereas measurements collected in 2025 were used as an independent test dataset. In addition, data from 2019 to 2023 were used for an additional temporal reproducibility assessment. During the 2019–2025 period, the Vaulx-en-Velin station provided online measurements at 1-min intervals. These data were first filtered using the standard CIE [28] quality control. Moreover, invalid records and data for which the solar altitude was lower than 5° were removed. Fig. 1 presents an exploratory Pearson correlation analysis between the candidate radiometric, atmospheric, and geometric variables and the global vertical illuminance measured on the east-, west-, north-, and south-facing façades in the 2024 training dataset.

As can be observed in Fig. 1, for the east-facing façade, the highest positive correlations appear for Kt, DNI, cos(θ), GHI, BHI, and ε, indicating a clear influence of the direct component and the incidence geometry. D and m show negative correlations, consistent with more diffuse conditions or higher optical air mass. For the west-facing façade, the pattern is very similar to that observed for the east-facing façade: Kt, DNI, cos(θ), ε, BHI, and GHI dominate. This confirms that the east- and west-facing orientations are strongly conditioned by the available direct radiation and by the angle of incidence on the façade. On the other hand,

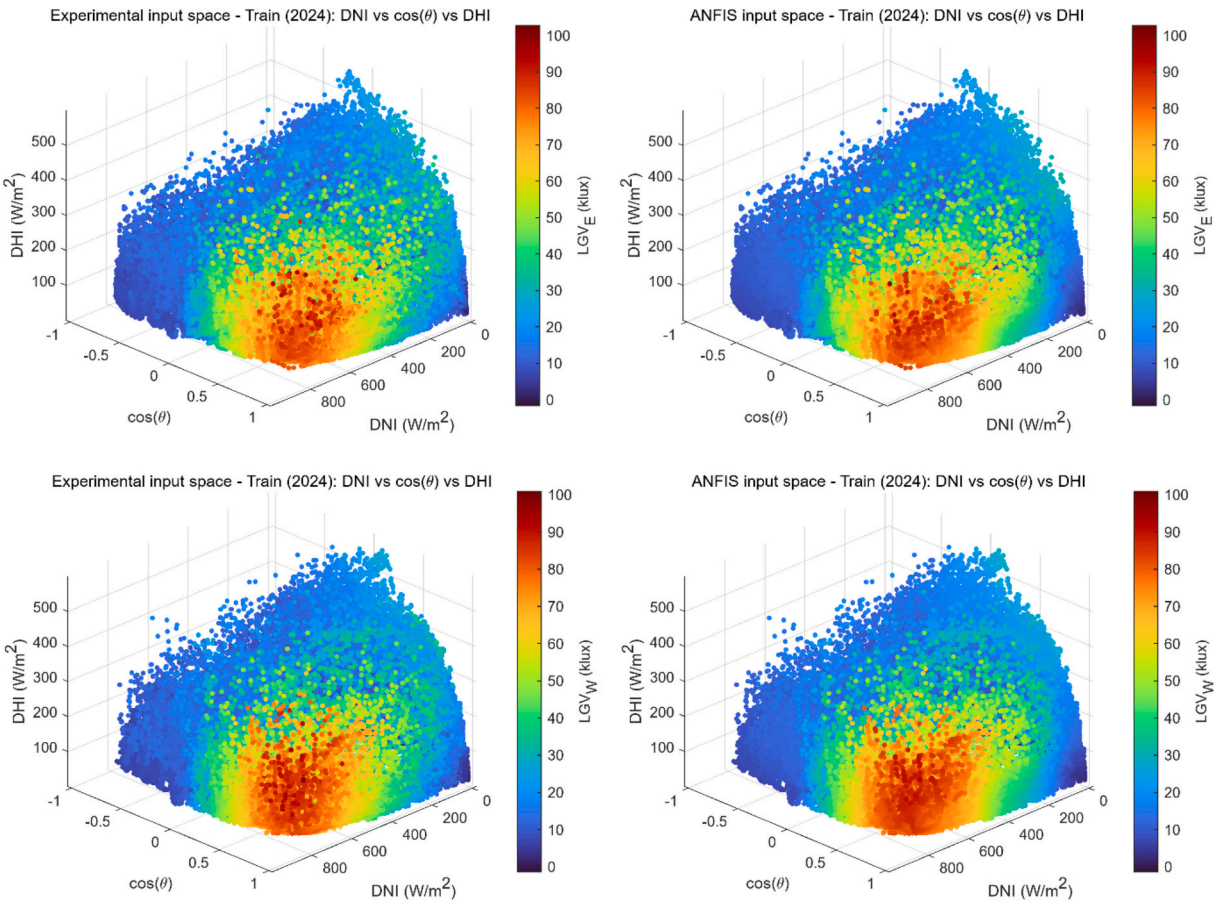


Fig. 8. Three-dimensional distribution of the DNI-cos(θ)-DHI input space, with experimental and ANFIS-estimated LGV values represented by color, for the east- and west-facing orientations in the training dataset (2024).

for the north-facing façade, the highest correlation corresponds to DHI, followed by zenith luminance, solar altitude, GHI, and Δ. This is physically consistent, since the north-facing façade receives little or no direct component for much of the time, so its vertical illuminance mainly depends on diffuse sky light. Finally, for the south-facing façade, the highest positive correlations are observed for Kt, GHI, DNI, BHI, and ε. This reflects the predominance of clear-sky conditions and direct radiation, although incidence geometry remains important.

The lower Pearson correlations between DHI and LGV for the east-, west-, and south-facing façades indicate that the diffuse component is not the dominant source of their annual linear variability. However, these lower Pearson coefficients do not demonstrate that DHI lacks predictive information. The predictor set was selected by combining physical relevance, availability at radiometric stations, and the objective of using a common input structure for four independently trained orientation-specific ANFIS models. Consequently, each model uses DNI, DHI, and the value of cos(θ) calculated for the corresponding façade. DNI and cos(θ) jointly describe the available direct component and its incidence geometry, whereas DHI provides information on the diffuse sky component, which is relevant in the present study because diffuse vertical illuminance measurements were not available. DHI was retained for all four orientations because the models were designed to estimate LGV under all-sky conditions. DNI and cos(θ) alone cannot distinguish observations with similar direct-radiation and geometric conditions but different diffuse levels. DHI is particularly informative under overcast and partly cloudy conditions, when DNI is low, and when cos(θ) is negative. When $\cos(\theta) < 0$, the Sun is behind the façade, so the direct beam contribution on the outward-facing vertical surface is zero. However, diffuse sky light, as well as reflected light from the surroundings, may still contribute to the global vertical illuminance, and therefore LGV may remain positive. Although DHI is not equivalent to diffuse irradiance on the vertical plane, it is a commonly available indicator of diffuse sky availability. Since the four ANFIS models were trained independently, each model can learn a different nonlinear relationship between DHI and LGV through its membership functions and fuzzy-rule consequents.

Variables such as GHI, BHI, Kt, ε, and D were not included because they combine or duplicate radiometric information already represented by DNI and DHI, or are derived from it. Their inclusion would increase the dimensionality and complexity of the ANFIS models. The selected variables therefore provide a common and physically grounded representation of the direct component, the diffuse component, and the orientation-specific incidence geometry, while limiting the number of model inputs.

The derived radiometric and geometric variables used in Fig. 1 were calculated using Eqs. (1)–(7). The incidence angle was calculated from the general expression for a tilted surface, shown in Eq. (1), where Z is the solar zenith angle, γ_s is the solar azimuth angle, and γ is the façade azimuth angle [29]. In Eq. (1), θ is the angle between the solar beam and the surface normal for a surface inclined in an arbitrary direction. For vertical façades, $\beta = 90°$; therefore, cos(θ) represents the geometric projection factor of the direct solar beam onto the vertical façade.

$$cos(\theta) = cos(Z)cos(\beta) + sin(Z)sin(\beta)cos(\gamma_s - \gamma) \quad (1)$$

The clearness index (Kt), which is defined as the ratio of horizontal global irradiance at ground level to horizontal extraterrestrial irradiance, was calculated using Eq. (2),

$$Kt = \frac{GHI}{I_0\, sin(\alpha)} \quad (2)$$

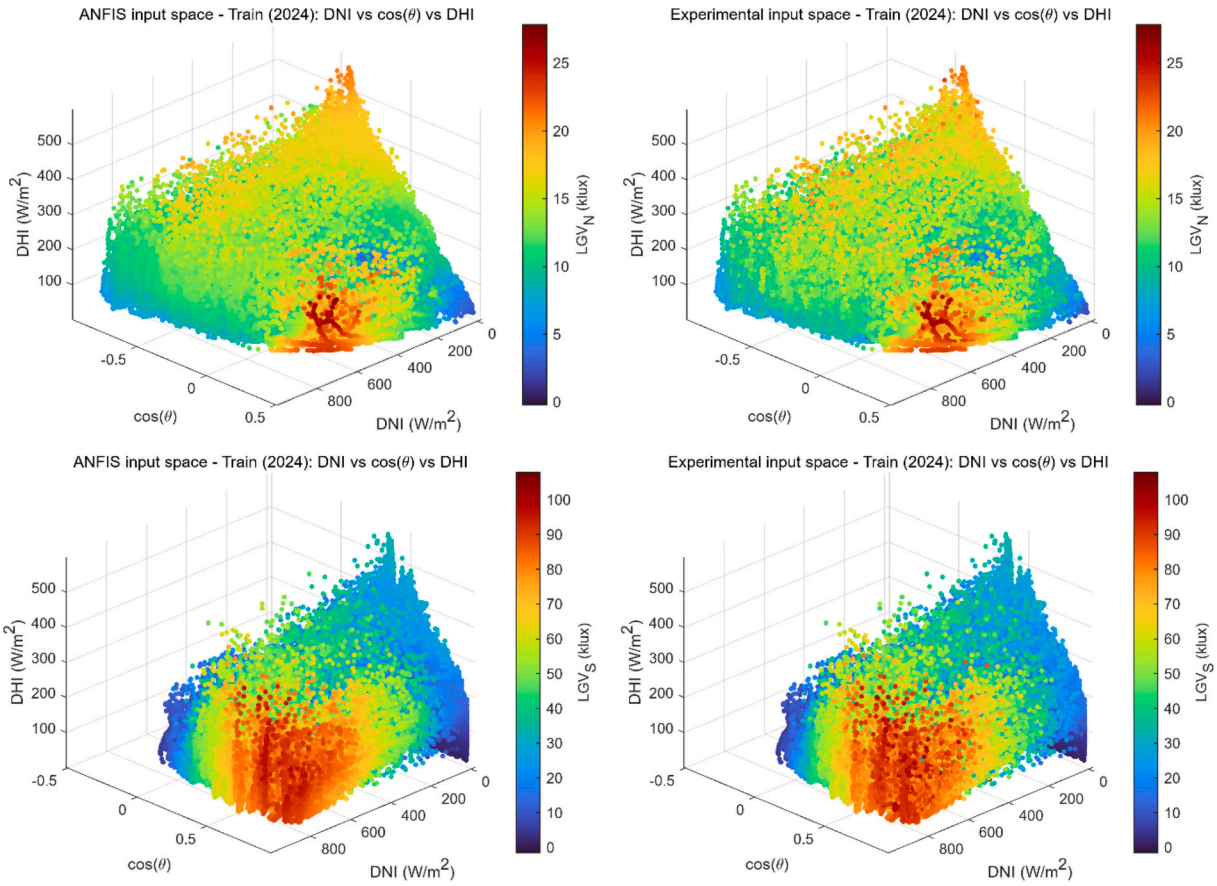


Fig. 9. Three-dimensional distribution of the DNI-cos(θ)-DHI input space, with experimental and ANFIS-estimated LGV values represented by color, for the north- and south-facing orientations in the training dataset (2024).

where α is the solar altitude angle. The extraterrestrial normal irradiance, I_0, is given by Eq. (3), and $I_{sc} = 1361.1\ W/m^2$ corresponds to the solar constant [30]. In addition, E_0 is the correction factor for the Sun-Earth distance, as shown in Eq. (4).

$$I_0 = I_{sc}\, E_0 \tag{3}$$

$$E_0 = 1 + 0.033 cos\left(\frac{2\pi d_n}{365}\right) \tag{4}$$

On the other hand, sky clearness (ε) is defined by Eq. (5), as proposed by Perez et al. [31], where Z is the solar zenith angle in radians. Likewise, the sky brightness (Δ) [31] is given by Eq. (6).

$$\varepsilon = \left(\frac{DHI + DNI}{DHI} + 1.041Z^3\right) \Big/ \left(1 + 1.041Z^3\right) \tag{5}$$

$$\Delta = \frac{mDHI}{I_0} \tag{6}$$

Moreover, the diffuse fraction (D), which is defined as the ratio of horizontal diffuse irradiance to horizontal global irradiance, can be obtained from Eq. (7).

$$D = \frac{DHI}{GHI} \tag{7}$$

2.2. Statistical metrics for model evaluation

Model performance was evaluated using nRMSE (%), nMBE (%), and nMAE (%), which were selected as the main comparative error metrics in this study. Eqs. (8)–(10) show these statistics, where y_j denotes the measured values, and $\hat{y}_j$ denotes the corresponding estimated values, and n denotes the number of data points.

$$nRMSE\ (\%) = 100\frac{RMSE}{\bar{y}}, where\ RMSE = \sqrt{\frac{\sum_{j=1}^{n}\left(\hat{y}_j - y_j\right)^2}{n}}, and\ \bar{y} = \frac{1}{n}\sum_{j=1}^{n} y_j \tag{8}$$

$$nMBE\ (\%) = 100\frac{\sum_{j=1}^{n}\left(\hat{y}_j - y_j\right)}{\sum_{j=1}^{n} y_j} \tag{9}$$

$$nMAE(\%) = 100\frac{MAE}{\bar{y}}, where\ MAE = \frac{1}{n}\sum_{j=1}^{n}\left|\hat{y}_j - y_j\right|, and\ \bar{y} = \frac{1}{n}\sum_{j=1}^{n} y_j \tag{10}$$

The coefficient of determination shown in Eq. (11) and Willmott's index of agreement (IA) shown in Eq. (12) were also used. IA ranges from 0 to 1, where 1 indicates perfect agreement, and provides an overall measure of the discrepancies between observations and estimates [33].

$$R^2 = 1 - \frac{\sum_{j=1}^{n}\left(y_j - \hat{y}_j\right)^2}{\sum_{j=1}^{n}\left(y_j - \bar{y}\right)^2} \tag{11}$$

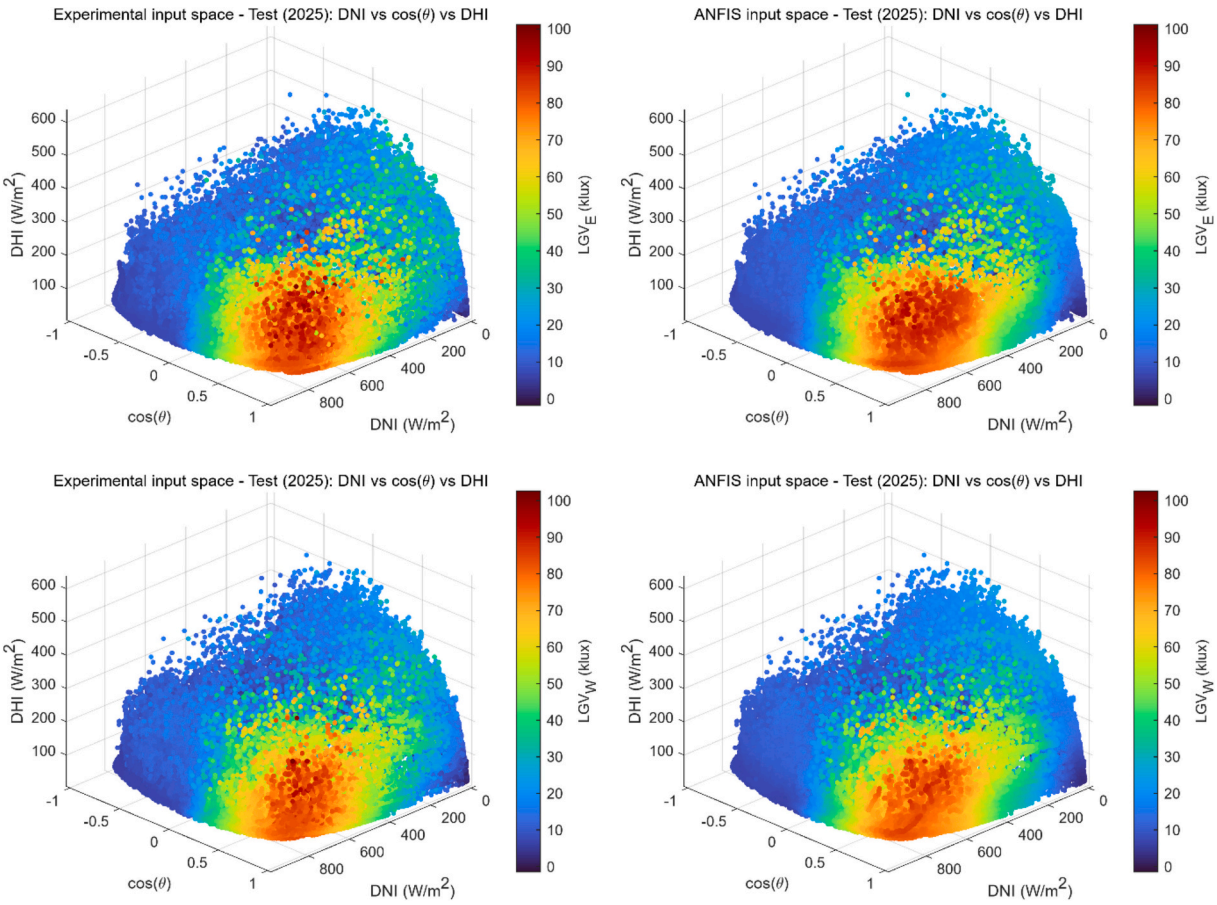


Fig. 10. Three-dimensional distribution of the DNI-cos(θ)-DHI input space, with experimental and ANFIS-estimated LGV values represented by color, for the east- and west-facing orientations in the test dataset (2025).

$$IA = 1 - \frac{\sum_{j=1}^{n}\left(\hat{y}_j - y_j\right)^2}{\sum_{j=1}^{n}\left(\left|\hat{y}_j - \bar{y}\right| + \left|y_j - \bar{y}\right|\right)^2} \tag{12}$$

2.3. Baseline model comparisons

Temporal robustness was assessed by training the models with data from 2024 and evaluating them on data from six independent years rather than on randomly mixed samples, thereby providing a more demanding test of model generalization under different interannual conditions. To provide a direct baseline comparison, the ANFIS models were compared with a feedforward artificial neural network and a quadratic response-surface regression model. For each method, the same three input configurations were considered: M1, based on DNI; M2, based on DNI and cos(θ); and M3, based on DNI, cos(θ), and DHI. All models used the same filtered records, predictors, training period, and independent evaluation periods. The models were trained using the 115,250 records from 2024 and evaluated using the 750,294 records from 2019 to 2023 and 2025. The six independent years were not used for architecture selection, hyperparameter adjustment, or selection of the best training run.

The ANN consisted of a feedforward network with one hidden layer, a hyperbolic tangent sigmoid transfer function in the hidden layer, and a linear output function. The ANN was trained using the scaled conjugate gradient algorithm. For each model configuration, the ANN used the same training and independent evaluation datasets and the same input and output variables as the corresponding ANFIS and regression models, while maintaining approximately equivalent numbers of trainable parameters. All valid records from 2024 were used for training, and the input normalization parameters derived exclusively from the 2024 dataset were subsequently applied to the independent years without recalculation. The number of hidden neurons was fixed before examining the independent evaluation results. Accordingly, M1, M2, and M3 used 4, 8, and 17 hidden neurons, respectively, as shown in Table 1, resulting in 13, 33, and 86 trainable parameters.

The regression baseline consisted of quadratic response surfaces fitted by ordinary least squares with an intercept. The models included linear terms, squared terms, and all two-factor interactions. The resulting M1, M2, and M3 models contained 3, 6, and 10 regression parameters, respectively, as shown in Table 1. These models are shown in Eqs. (13)–(15).

$$\mathrm{M1}: \widehat{\mathrm{LGV}} = \beta_0 + \beta_1\,\mathrm{DNI} + \beta_2\,\mathrm{DNI}^2 \tag{13}$$

$$\mathrm{M2}: \widehat{\mathrm{LGV}} = \beta_0 + \beta_1\,\mathrm{DNI} + \beta_2\cos(\theta) + \beta_3\,\mathrm{DNI}^2 + \beta_4\cos^2(\theta) + \beta_5\,\mathrm{DNI}\cos(\theta) \tag{14}$$

$$\begin{aligned}\mathrm{M3}: \widehat{\mathrm{LGV}} = {} & \beta_0 + \beta_1\,\mathrm{DNI} + \beta_2\cos(\theta) + \beta_3\,\mathrm{DHI} + \beta_4\,\mathrm{DNI}^2 + \beta_5\cos^2(\theta) \\ & + \beta_6\,\mathrm{DHI}^2 + \beta_7\,\mathrm{DNI}\cos(\theta) + \beta_8\,\mathrm{DNI}\,\mathrm{DHI} \\ & + \beta_9\cos(\theta)\,\mathrm{DHI}\end{aligned} \tag{15}$$

3. Modeling of global vertical solar illuminance

As previously mentioned, adaptive neuro-fuzzy inference systems (ANFIS) were used to model the global vertical illuminance measured on the four building façades. Four independent models were trained, cor-

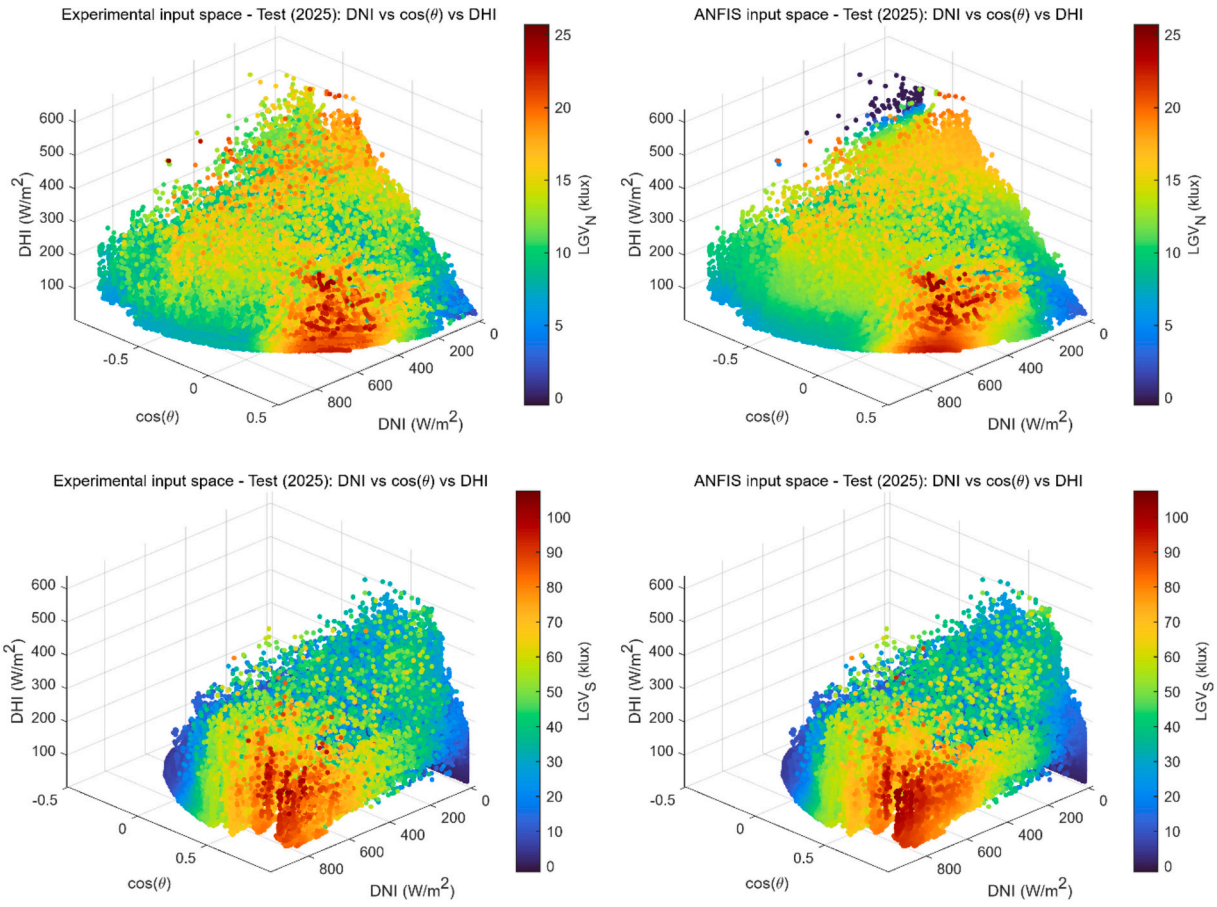


Fig. 11. Three-dimensional distribution of the DNI-cos(θ)-DHI input space, with experimental and ANFIS-estimated LGV values represented by color, for the north- and south-facing orientations in the test dataset (2025).

responding to the north-, east-, south-, and west-facing façades. In all cases, the same reduced set of input variables was used: direct normal irradiance (DNI), diffuse horizontal irradiance (DHI), and the cosine of the incidence angle, cos(θ), defined by Eq. (1). As indicated above, these variables were selected because they represent the main physical mechanisms governing vertical illuminance: the available direct component, the diffuse sky contribution, and the incidence geometry on each façade. The façade azimuth angles were defined as 0°, 90°, 180°, and 270° for the north-, east-, south-, and west-facing façades, respectively. Direct normal irradiance was calculated from beam horizontal irradiance, as shown in Eq. (16):

$$DNI = \frac{BHI}{sin(\alpha)} \tag{16}$$

where BHI is the beam horizontal irradiance. The initial fuzzy inference systems were generated by grid partitioning using the *genfis* function in Matlab® R2022b and the Fuzzy Logic Toolbox™ [27]. A zero-order Sugeno FIS was used [32], with Gaussian membership functions for the input variables and constant output functions. Gaussian membership functions were selected because they provide smooth transitions between fuzzy sets. The Gaussian membership function used for each input is defined as shown in Eq. (17).

$$\mu(x) = exp\left(-\frac{(x-c)^2}{2\sigma^2}\right) \tag{17}$$

where c and σ are the center and width of the Gaussian membership function, respectively. A type-1 fuzzy set can be defined over a universe X, as shown in Eq. (18):

$$A = \{(x, \mu_A(x)) | x \in X, 0 \le \mu_A(x) \le 1\} \tag{18}$$

where $\mu_A(x)$ represents the degree of membership of x in the fuzzy set A [27]. For each façade, the ANFIS model was constructed with three inputs and four Gaussian membership functions per input. In this configuration, the input space is divided into four fuzzy regions for each input variable, generating the initial membership functions and all possible combinations among them. As a result, grid partitioning generates $4^3 = 64$ fuzzy rules, each associated with a specific combination of input membership functions. These fuzzy rules have the general form shown in Eq. (19).

$$\text{If } (DNI \text{ is } A_i) \text{ and } (cos(\theta) \text{ is } B_j) \text{ and } (DHI \text{ is } C_k), \text{ then } LGV = c_{ijk} \tag{19}$$

where A_i, B_j and C_k are the fuzzy sets associated with DNI, cos(θ) and DHI, respectively, and c_{ijk} is the constant consequent of the corresponding zero-order Sugeno rule. For each rule, the firing strength (ω_l) was calculated as the product of the membership degrees, as shown in Eq. (20).

$$\omega_l = \mu_{A_i}(DNI)\, \mu_{B_j}(cos(\theta))\, \mu_{C_k}(DHI) \tag{20}$$

In Eq. (21), $\overline{\omega}_l$ represents the normalized firing strength of rule l, where $i,j,k = 1,\ldots,4$, and each combination (i,j,k) corresponds to one rule indexed by $l = 1,\ldots,64$.

$$\overline{\omega}_l = \frac{\omega_l}{\sum_{m=1}^{64} \omega_m} \tag{21}$$

Finally, the output of the zero-order Sugeno system was obtained as

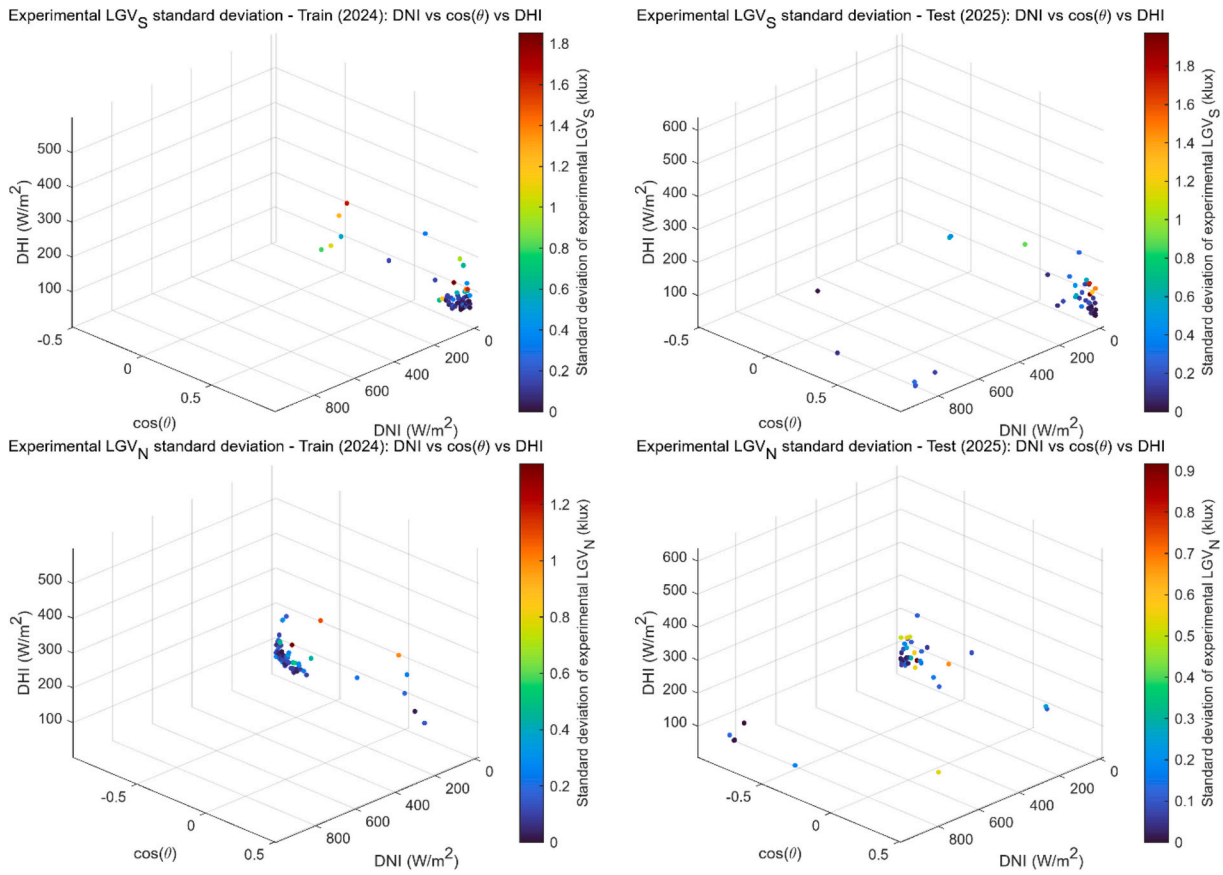


Fig. 12. Three-dimensional distribution of the standard deviation of experimental LGV for the N- and S-facing orientations in 2024 and 2025.

the weighted average of the constant consequents using Eq. (22), where $\hat{y}$ is the estimated global vertical illuminance (LGV).

$$\hat{y} = \widehat{LGV} = \sum_{m=1}^{64} \overline{\omega}_m c_m \tag{22}$$

Different ANFIS configurations were tested, including first-order Sugeno models with linear consequents and zero-order Sugeno models with constant consequents. Finally, a zero-order Sugeno configuration with four Gaussian membership functions per input was selected. This structure was chosen to maintain a balance between predictive capability, physical interpretability, and computational simplicity, avoiding an excessive increase in the number of model parameters. ANFIS training was performed for 50 epochs, using an initial step size of 0.01, a step-size decrease rate of 0.9, and a step-size increase rate of 1.1. The predictor variables were used in their original scales without normalization. The ANFIS models were trained using data from 2024 and independently evaluated using data from 2019 to 2023 and 2025. Fig. 2 shows the architecture of the constant Sugeno FIS used in the ANFIS models. The system uses three input variables, each described by four Gaussian membership functions. In the rule layer, the firing strength ω_l is calculated as the product of the membership degrees. These firing strengths are then normalized to obtain $\overline{\omega}_l$. Since this is a zero-order Sugeno system, each rule has a constant consequent c_l, so that the final output is obtained as the weighted sum of the constant consequents.

Since global vertical illuminance cannot take physically negative values, the negative predictions generated by the ANFIS models for estimating global vertical illuminance on façades were truncated to zero, as shown in Eq. (23). Based on the above, four ANFIS models were developed, one for each orientation, so that, using a similar scheme, global vertical illuminance values were obtained for the four cardinal orientations (N, E, S, and W).

$$\mathrm{LGV_j} = \max\left\{0, \hat{y}_{\mathrm{ANFIS,j}}\right\}, \text{where } \mathrm{j} \in \{\mathrm{N, E, S, W}\} \tag{23}$$

Across the six independent evaluation years, negative predictions occurred only for the north-facing façade: 79 cases, corresponding to 0.0105% of the north-facing predictions. No negative predictions occurred for the east-, south-, or west-facing façades. For the north-facing façade, truncation to zero reduced nRMSE and nMAE, corresponding to relative reductions of 1.63% and 0.17%, respectively, confirming that its influence on the overall results was very small.

The comparison between the initial and trained membership functions shown in Fig. 3 indicates that ANFIS training produced only slight changes in the premise parameters. The general shape and distribution of the input membership functions remain almost unchanged, indicating that the model adjustment was mainly performed through the consequent parameters rather than by substantially modifying the input fuzzy partitions.

Figs. 4-7 show the comparison between the experimental values of global vertical illuminance under all-sky conditions, for the four orientations considered, and the results obtained using the proposed ANFIS models. As indicated above, these models were developed from three variables that can be easily obtained at conventional measurement stations: direct normal irradiance, diffuse horizontal irradiance, and the cosine of the angle of incidence on the façade.

Fig. 4 shows a good agreement between the experimental and estimated values of global vertical illuminance for the east-facing orientation (LGV_E), for both the training and testing datasets. The coefficients of determination are high in both cases, with $R^2 = 0.9823$ for 2024 and $R^2 = 0.9882$ for 2025, indicating the high predictive capability of the model. The slope close to 1 confirms that the estimates adequately follow the trend of the experimental data. A high level of fit is also observed for the west-facing orientation in Fig. 5 and for the south-

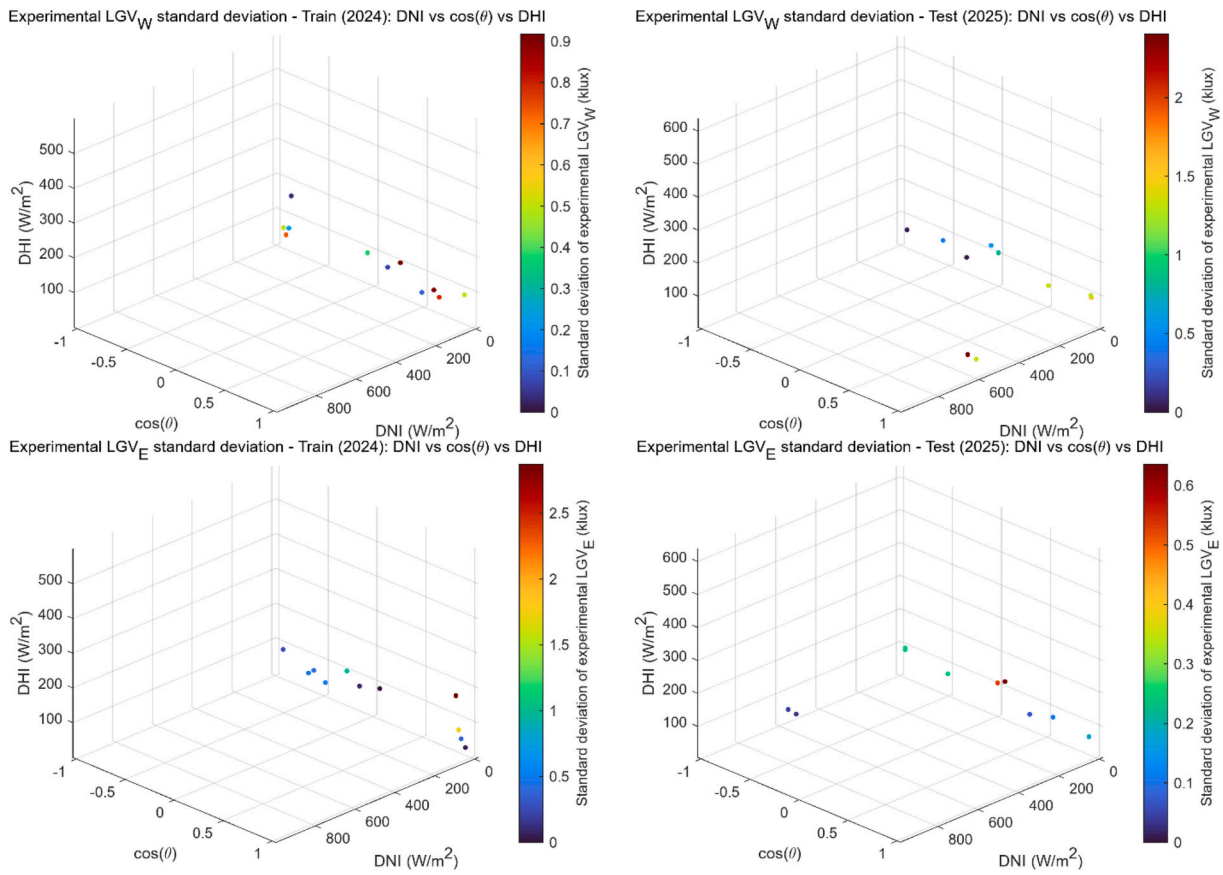


Fig. 13. Three-dimensional distribution of the standard deviation of experimental LGV for the *E*- and W-facing orientations in 2024 and 2025.

facing orientation in Fig. 6, with R^2 values close to or greater than 0.98 and slopes close to 1, confirming the good stability of the model between training and testing. Likewise, for the north-facing orientation, shown in Fig. 7, although the fit is somewhat lower and the dispersion is greater, the model still adequately reproduces the general trend of the experimental data.

4. Results and discussion

This section presents and discusses the results obtained with the proposed ANFIS approach. First, the influence of the selected input variables on model performance is examined, followed by an analysis of the two-dimensional response curves and three-dimensional response surfaces. The statistical performance of the final ANFIS models is then evaluated using the 2024 training dataset and the six independent evaluation years, 2019–2023 and 2025. Their performance is subsequently compared with that obtained using quadratic response-surface regression and ANN models. Finally, the errors are analyzed under different sky, seasonal, and solar-geometry conditions to identify the situations associated with increased dispersion or systematic bias.

4.1. Influence of the selected input variables on ANFIS performance

To determine the influence of DHI on LGV prediction, its contribution was first evaluated by comparing the reduced M2 model, based on DNI and cos(θ), with the complete M3 model, based on DNI, cos(θ), and DHI. Both models were trained using the 2024 data and evaluated using exactly the same 750,294 records corresponding to the six independent years. The results are shown in Table 2.

As shown in Table 2, incorporating DHI into the models reduced both nRMSE and nMAE for all four orientations. The relative reduction in nRMSE ranged from 46.4% to 59.5%, whereas that in nMAE ranged from 56.5% to 64.7%. The greatest improvement was obtained for the north-facing façade, which is consistent with the greater relative contribution of diffuse radiation to this orientation. In addition, both errors decreased in all 24 combinations formed by the four orientations and the six independent years. Therefore, the improvement was not specific to a particular orientation or year, and the results quantitatively support retaining DHI as a predictor.

The remaining metrics also improved when DHI was included in the models. Specifically, nMBE decreased from 2.17% to 0.85% for the east-facing façade, from 2.01% to 0.71% for the west-facing façade, from 6.12% to 2.66% for the north-facing façade, and from 2.39% to 0.68% for the south-facing façade. Similarly, R^2 increased from 0.95 to 0.98, from 0.96 to 0.99, from 0.38 to 0.90, and from 0.94 to 0.99, respectively. IA increased from 0.99 to 1.00 for the east-, west-, and south-facing façades and from 0.75 to 0.97 for the north-facing façade. Furthermore, DHI represents the availability of diffuse sky radiation, which cannot be determined using DNI and cos(θ) alone. When cos(θ) is negative, the Sun is behind the façade plane and there is no direct solar incidence, although LGV may remain significant because of diffuse daylight. In addition, DHI is more commonly available at radiometric stations than vertical diffuse irradiance, allowing LGV to be estimated without requiring additional vertical measurements. Based on the above, DNI, cos(θ), and DHI were selected as the final model inputs.

4.2. Analysis of ANFIS response surfaces

The results obtained for the *E*-, W-, N-, and S-facing orientations using the ANFIS models described in the previous section are presented. The experimental input-output domain was visualized with DNI, DHI, and cos(θ) represented on the three spatial axes and global vertical illuminance (LGV) encoded by color. Each point corresponds to an exact combination of DNI, DHI, and cos(θ). When two or more experimental

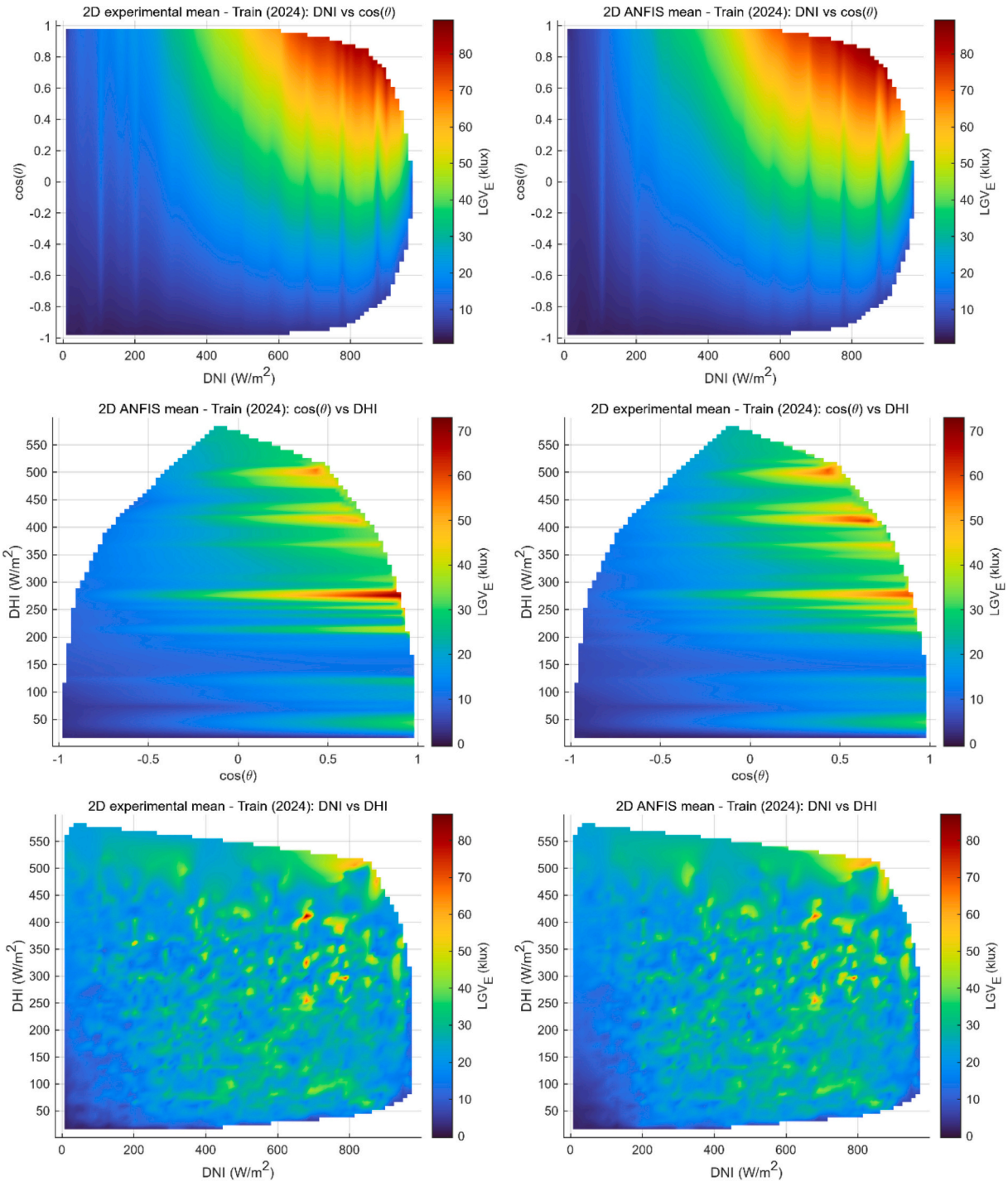


Fig. 14. 2D projections of the input space and mean experimental and ANFIS-estimated LGV_E values for the training dataset (2024): DNI-cos(θ), cos(θ)-DHI, and DNI-DHI.

observations had exactly identical values of the three inputs, their LGV measurements were averaged to avoid the overlap of coincident points. Input combinations occurring only once retained their original experimental LGV value. Because ANFIS is deterministic, identical input combinations produce the same estimated LGV value.

Fig. 8 shows the three-dimensional distribution of the input space defined by DNI, DHI, and cos(θ), with experimental and ANFIS-estimated LGV values represented by color for the east- and west-facing orientations in the 2024 training dataset. Both orientations exhibit similar response patterns, consistent with their comparable incidence geometry relative to the daily solar path, although the direct contribution is concentrated in the morning for the east-facing façade and in the afternoon for the west-facing façade. Higher LGV values generally occur when high DNI coincides with large positive values of cos(θ), reflecting the combined effect of available direct radiation and favorable incidence geometry. DHI accounts for the diffuse contribution throughout the input domain, including conditions in which the direct component is limited by the façade orientation.

Fig. 9 shows the three-dimensional distribution of the input space defined by DNI, DHI, and cos(θ) with experimental and ANFIS-estimated LGV values represented by color for the north- and south-facing orientations in the 2024 training dataset. The two orientations exhibit clearly

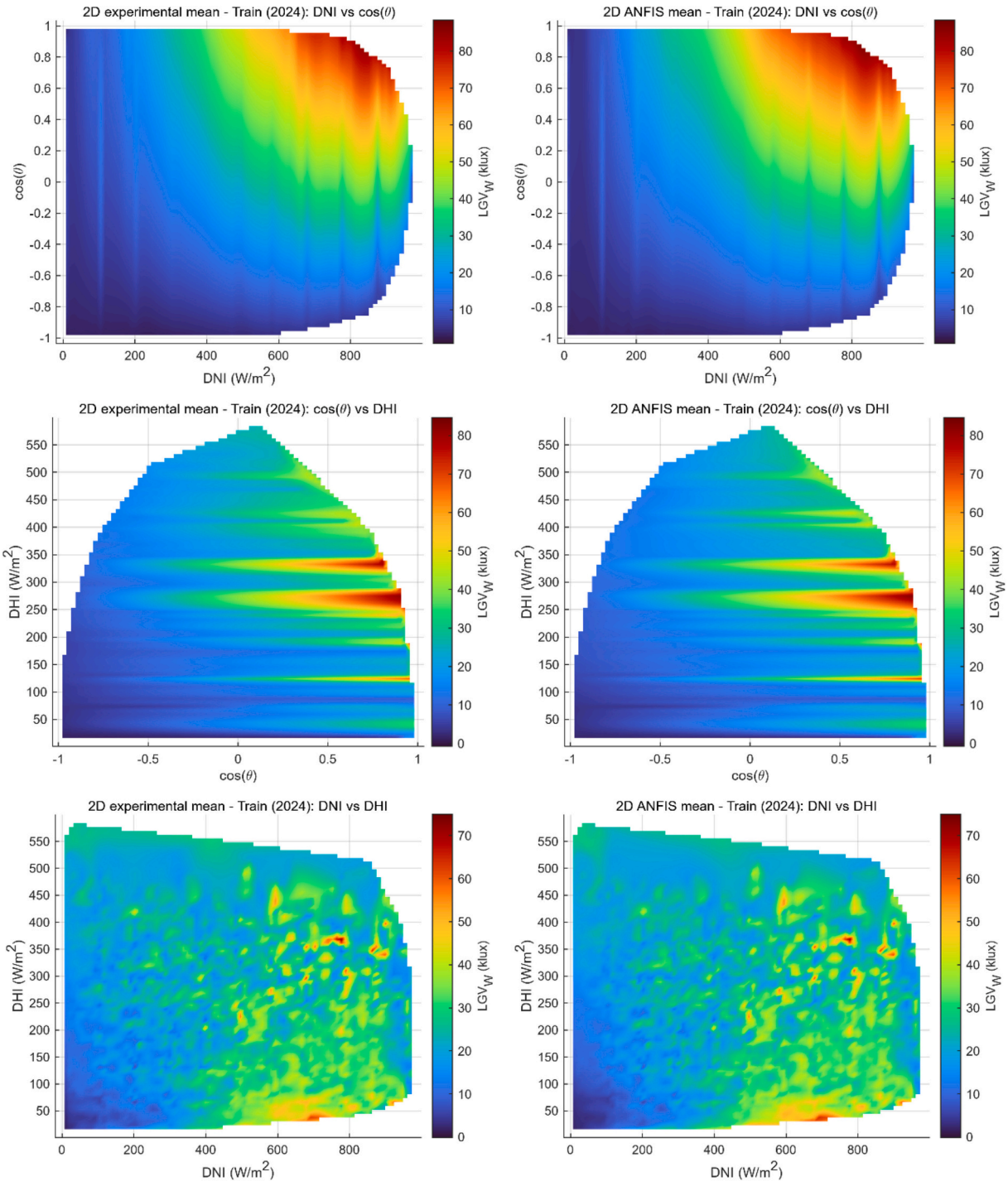


Fig. 15. 2D projections of the input space and mean experimental and ANFIS-estimated LGV_W values for the training dataset (2024): DNI-cos(θ), cos(θ)-DHI, and DNI-DHI.

different response patterns. The north-facing façade presents lower LGV values, consistent with its limited direct solar contribution and the greater relative importance of diffuse radiation. In contrast, the south-facing façade reaches higher LGV values, particularly when high DNI coincides with large positive values of cos(θ), indicating favorable incidence geometry. Compared with the east- and west-facing façades, the south-facing orientation exhibits a broader region of high LGV values, whereas the north-facing façade presents the lowest illuminance levels.

Fig. 10 shows the three-dimensional distributions for the east- and west-facing orientations in the 2025 independent test dataset. Their general patterns are similar to those observed for the 2024 training dataset in Fig. 8. Higher LGV values generally occur when high DNI coincides with positive and high cos(θ), whereas lower values are associated with less favorable incidence geometry.

Fig. 11 shows that, in the 2025 test dataset, the three-dimensional distributions for the north- and south-facing orientations maintain a structure very similar to that observed in the 2024 training data, shown in Fig. 9. For the north-facing orientation, LGV values remain lower and dominated by a more diffuse response, whereas for the south-facing orientation, the higher-illuminance regions associated with high DNI and cos(θ) values are preserved.

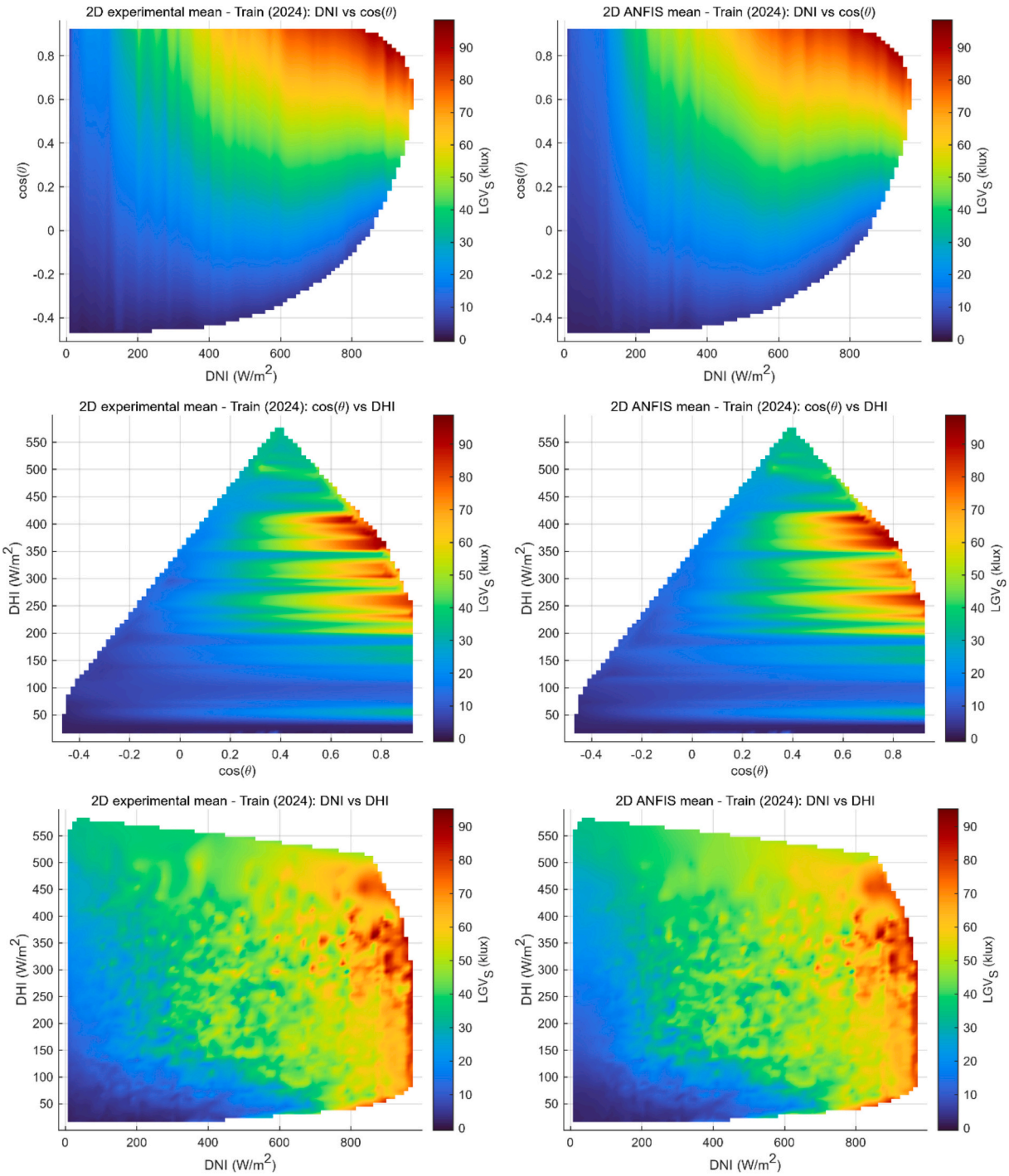


Fig. 16. 2D projections of the input space and mean experimental and ANFIS-estimated LGV_S values for the training dataset (2024): DNI-cos(θ), cos(θ)-DHI, and DNI-DHI.

To characterize the experimental dispersion associated with identical combinations of DNI, DHI, and cos(θ), the standard deviation of the measured LGV values was calculated. Figs. 12 and 13 show the exact combinations that occurred more than once. No equivalent representation is included for ANFIS because, as a deterministic model, it assigns a single output to each input combination. As can be observed, the standard deviation of experimental LGV is generally low, with only a few localized values of greater magnitude. No extensive region of the input space exhibits high variability. Therefore, averaging coincident observations does not conceal substantial local dispersion and supports the qualitative interpretation of the color distributions shown in Figs. 8–11. The standard deviations of the ANFIS estimates were not included because, as deterministic models, they produce identical values under identical input conditions.

In addition to the results shown in Figs. 8–11, two-dimensional projections were included to assess whether the trends estimated by ANFIS reproduce those observed in the experimental LGV values averaged within each cell of the projected input space, thereby facilitating comparison between the experimental data and the model estimates. Fig. 14 shows the two-dimensional projections of the input space for the east-facing orientation, comparing the mean experimental and estimated LGV_E values. The DNI-cos(θ) projection clearly shows the

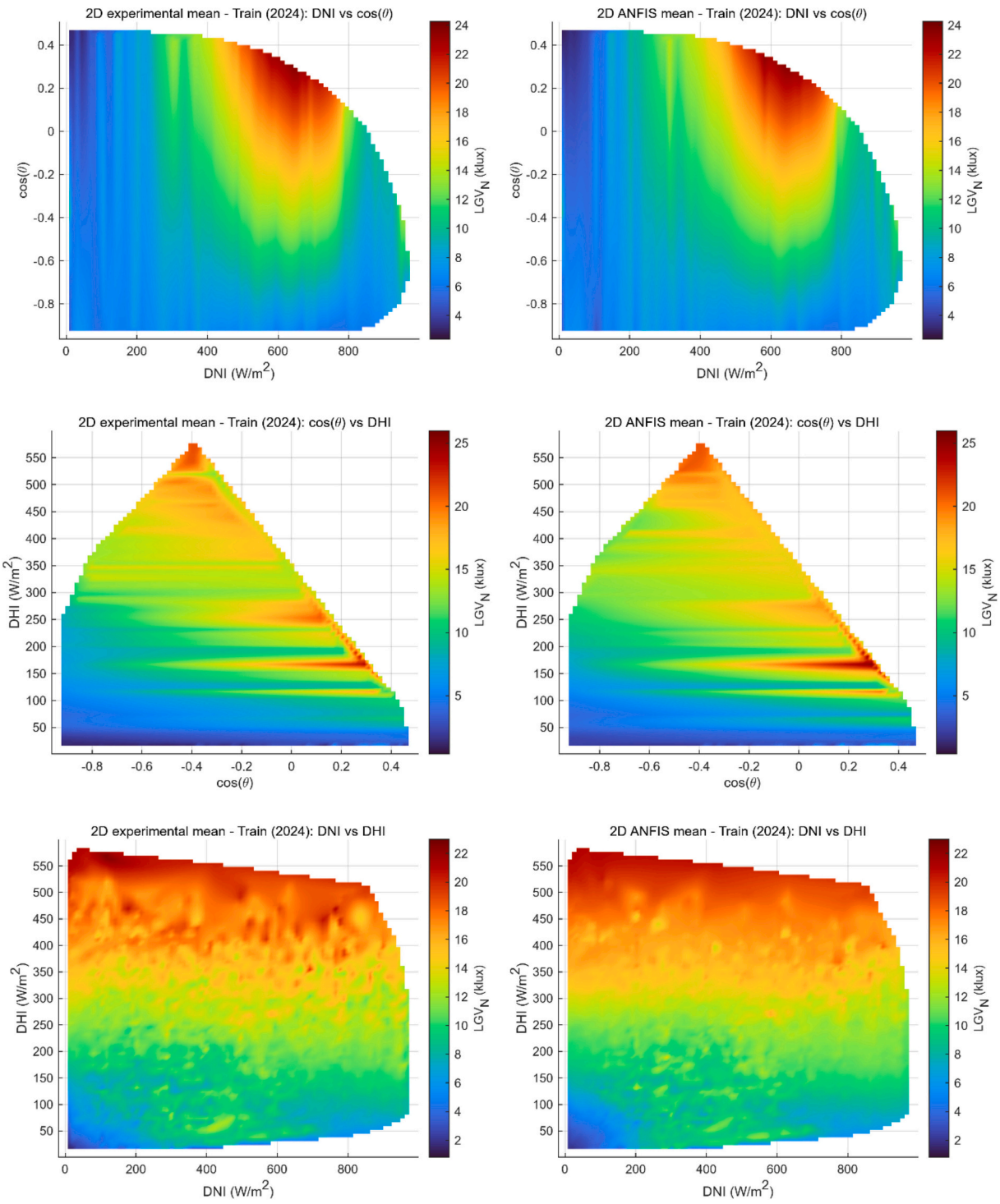


Fig. 17. 2D projections of the input space and mean experimental and ANFIS-estimated LGV_N values for the training dataset (2024): DNI-cos(θ), cos(θ)-DHI, and DNI-DHI.

Table 3
Normalized performance metrics of the ANFIS models for the 2024 training dataset in the four orientations.

Orientation	nRMSE (%)	nMBE (%)	nMAE (%)	R^2	IA
E	16.3799	0.0000	9.6963	0.9823	0.9955
W	13.2359	0.0000	8.3114	0.9882	0.9970
N	13.2844	0.0000	9.6002	0.9338	0.9826
S	12.2176	0.0000	7.5422	0.9885	0.9971

Table 4
Normalized performance metrics of the ANFIS models for the 2025 independent test dataset in the four orientations.

Orientation	nRMSE (%)	nMBE (%)	nMAE (%)	R^2	IA
E	12.7619	−0.4812	7.3155	0.9882	0.9970
W	12.0687	0.0368	7.4817	0.9899	0.9974
N	15.4101	−1.4233	9.5110	0.8964	0.9725
S	12.0921	0.8134	7.2552	0.9844	0.9962

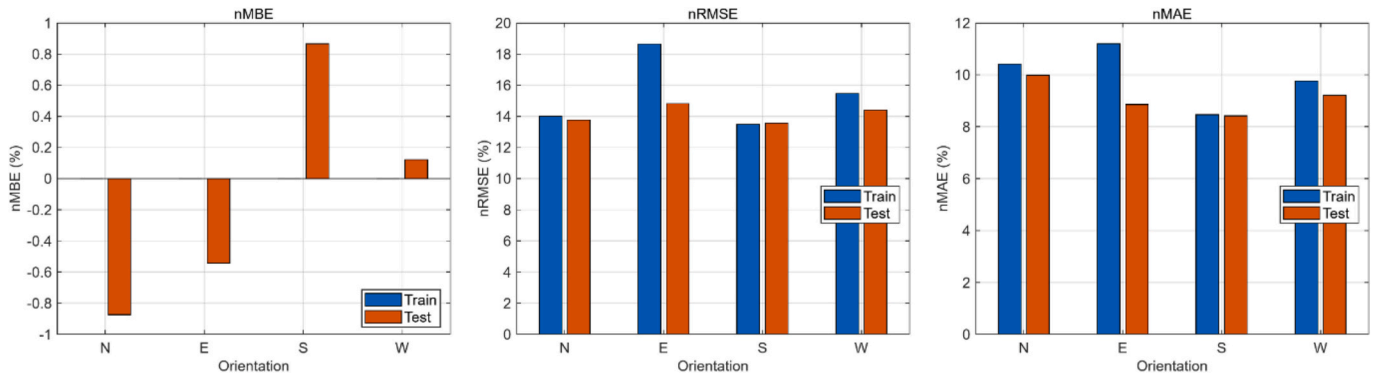


Fig. 18. Comparison of the nRMSE, nMBE, and nMAE performance metrics for the training (2024) and test (2025) datasets in the four orientations.

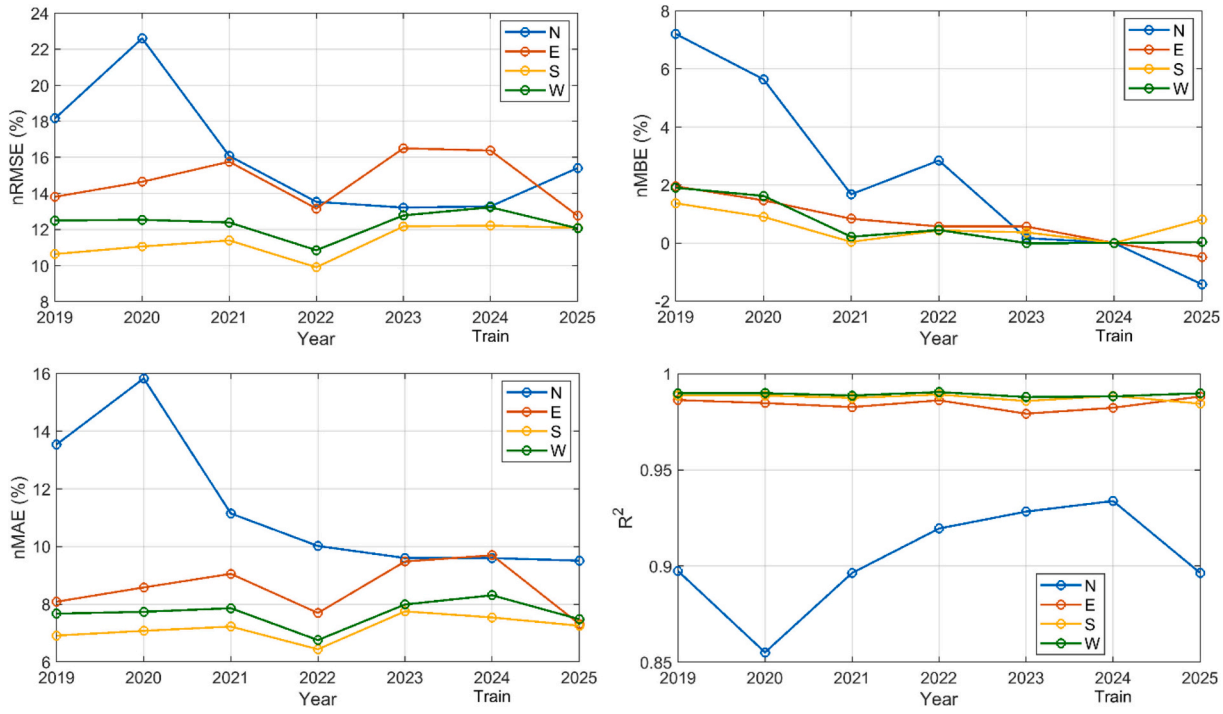


Fig. 19. Annual evolution of nRMSE (%), nMBE (%), nMAE (%), and R^2 for the ANFIS models from 2019 to 2025 for the four vertical orientations: north (N), east (E), south (S), and west (W). The year 2024 corresponds to the training year, and 2019–2023 and 2025 correspond to the testing years.

Table 5
Normalized performance metrics of the ANFIS models for 2019.

Orientation	nRMSE (%)	nMBE (%)	nMAE (%)	R^2	IA
N	18.1611	7.2043	13.5371	0.8975	0.9729
E	13.8149	1.9544	8.0893	0.9863	0.9966
S	10.6400	1.3709	6.9144	0.9887	0.9972
W	12.4997	1.9048	7.6751	0.9899	0.9975

Table 6
Normalized performance metrics of the ANFIS models for 2020.

Orientation	nRMSE (%)	nMBE (%)	nMAE (%)	R^2	IA
N	22.5976	5.6428	15.8250	0.8551	0.9596
E	14.6454	1.4721	8.5824	0.9847	0.9962
S	11.0609	0.9010	7.0797	0.9886	0.9972
W	12.5398	1.6252	7.7389	0.9899	0.9975

Table 7
Normalized performance metrics of the ANFIS models for 2021.

Orientation	nRMSE (%)	nMBE (%)	nMAE (%)	R^2	IA
N	16.0821	1.6785	11.1461	0.8964	0.9726
E	15.7601	0.8377	9.0539	0.9826	0.9957
S	11.3958	0.0409	7.2270	0.9874	0.9969
W	12.3923	0.2169	7.8628	0.9887	0.9971

Table 8
Normalized performance metrics of the ANFIS models for 2022.

Orientation	nRMSE (%)	nMBE (%)	nMAE (%)	R^2	IA
N	13.5361	2.8444	10.0191	0.9195	0.9789
E	13.1617	0.5697	7.6990	0.9862	0.9965
S	9.9087	0.4349	6.4406	0.9892	0.9973
W	10.8542	0.4496	6.7586	0.9905	0.9976

Table 9
Normalized performance metrics of the ANFIS models for 2023.

Orientation	nRMSE (%)	nMBE (%)	nMAE (%)	R^2	IA
N	13.2161	0.1707	9.6024	0.9283	0.9809
E	16.5043	0.5671	9.4815	0.9792	0.9948
S	12.1706	0.3678	7.7546	0.9858	0.9965
W	12.7815	−0.0038	7.9924	0.9879	0.9969

increase in LGV associated with high values of both variables, while the cos(θ)-DHI and DNI-DHI projections reflect the contribution of the diffuse component under different geometric conditions.

The similarity between the experimental maps and those obtained using ANFIS confirms that the model adequately reproduces the mean patterns observed in the input space. The figure shows that high DNI values do not necessarily imply high vertical illuminance values on the east-facing façade. DNI represents the direct radiation available in the direction of the Sun, measured normal to the solar beam, but by itself it does not indicate whether this radiation effectively strikes a specific façade. For the direct component to contribute effectively to LGV_E, high DNI must coincide with favorable incidence geometry, that is, with positive and high values of cos(θ). When cos(θ) is low, close to zero, or negative, direct radiation is not effectively projected onto the east-facing façade, even if DNI is high. Under these conditions, LGV_E remains low or is mainly dominated by the diffuse component.

Fig. 15 shows, for the west-facing orientation, a pattern very similar to that previously observed for the east-facing façade. This similarity is consistent with the comparable geometric behavior of both orientations, since in each case cos(θ) is calculated with respect to the corresponding façade. Therefore, although the direct contribution occurs at different times of the day, the relationship among DNI, DHI, cos(θ), and LGV shows a similar structure for both façades. In addition, the correspondence between the experimental maps and those estimated using ANFIS

Table 10
Absolute RMSE and MAE values (lux) of the ANFIS models for the four façade orientations during the training year (2024) and the six independent evaluation years (2019–2023 and 2025).

Year	RMSE (lux)				MAE (lux)			
	E	W	N	S	E	W	N	S
2019	2607.6	2177.4	1274.4	2648.9	1526.9	1337.0	949.9	1721.4
2020	2606.9	2154.8	1637.7	2607.2	1527.6	1329.8	1146.9	1668.8
2021	2583.6	2361.1	1275.6	2567	1484.2	1498.1	884.1	1628
2022	2561.9	2375.4	1104.7	2572.7	1498.6	1479.1	817.7	1672.3
2023	2915.1	2411.2	1086.1	2823.1	1674.7	1507.7	789.1	1798.8
2024	2315.8	2130.5	1032.2	2420.4	1370.9	1337.8	745.9	1494.2
2025	2470.3	2202.2	1287.7	2565.3	1416.1	1365.2	794.8	1539.2

Table 11
Comparison of the M3 models over the six independent evaluation years.

Orientation	Method	nRMSE (%)	nMBE (%)	nMAE (%)	R^2	IA
East	ANFIS	14.4414	0.8200	8.3703	0.9845	0.9961
East	ANN	15.7019	0.9396	9.7987	0.9820	0.9955
East	Regression	32.8755	−0.3899	25.0765	0.9205	0.9788
West	ANFIS	12.1894	0.7049	7.5849	0.9894	0.9973
West	ANN	14.4013	1.1422	9.8951	0.9853	0.9963
West	Regression	32.3135	−0.5440	24.5721	0.9259	0.9805
North	ANFIS	16.5005	2.6862	11.6068	0.8989	0.9729
North	ANN	18.4973	2.6201	13.1748	0.8746	0.9653
North	Regression	24.2395	2.9718	17.1124	0.7814	0.9354
South	ANFIS	11.2113	0.6548	7.1119	0.9873	0.9969
South	ANN	11.4125	0.5829	7.7893	0.9871	0.9968
South	Regression	14.1714	0.6069	10.0533	0.9798	0.9950

Table 12
Comparison of the M3 models for the 2024 training dataset.

Orientation	Method	nRMSE (%)	nMBE (%)	nMAE (%)	R^2	IA
East	ANFIS	16.3799	0.0000	9.6963	0.9823	0.9955
East	ANN	18.0805	0.2666	11.5266	0.9784	0.9945
East	Regression	37.0284	0.0000	28.1681	0.9095	0.9758
West	ANFIS	13.2359	0.0000	8.3114	0.9882	0.9970
West	ANN	15.6167	0.2694	10.3720	0.9836	0.9958
West	Regression	32.3109	0.0000	24.4598	0.9298	0.9815
North	ANFIS	13.2844	0.0000	9.6002	0.9338	0.9826
North	ANN	14.8044	−0.0164	10.5128	0.9178	0.9782
North	Regression	19.1094	0.0000	13.5485	0.8631	0.9620
South	ANFIS	12.2176	0.0000	7.5422	0.9885	0.9971
South	ANN	12.8788	0.1090	8.5051	0.9872	0.9968
South	Regression	15.1260	0.0000	10.5983	0.9824	0.9955

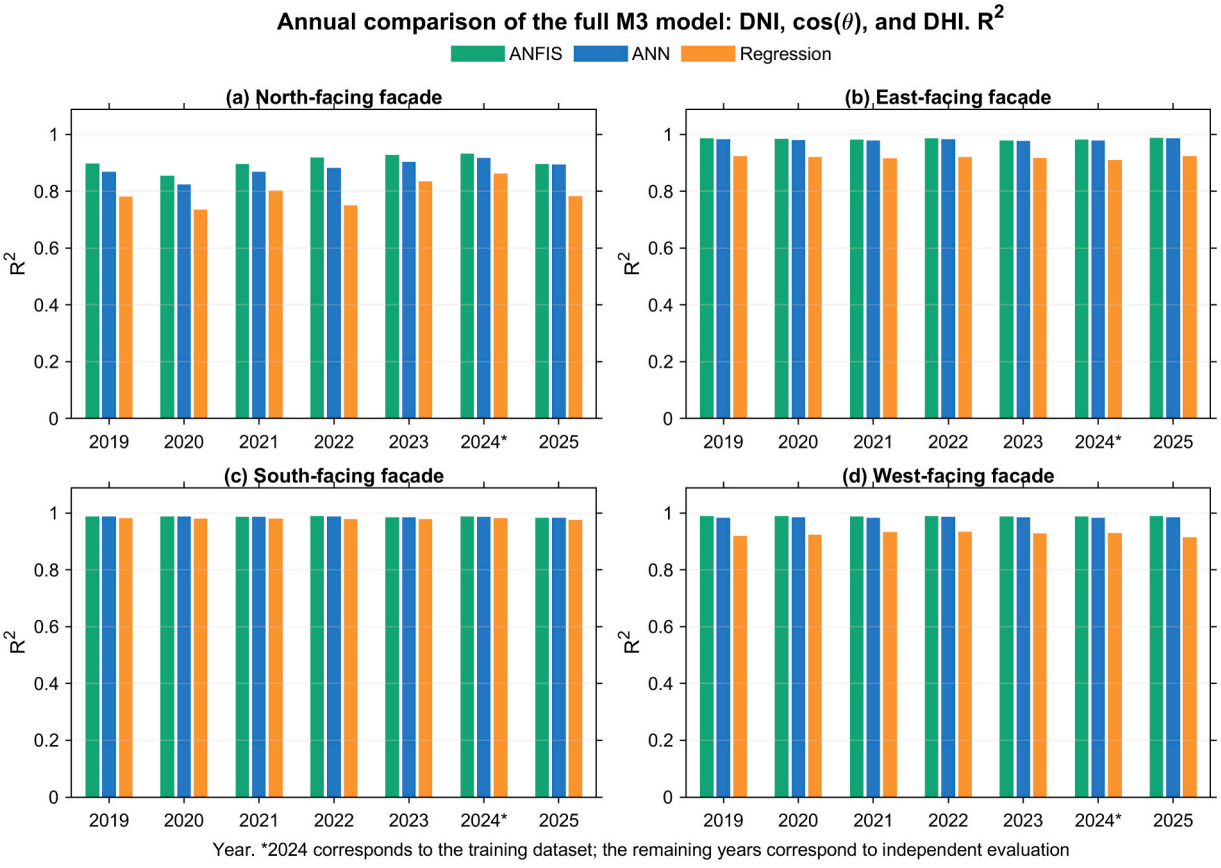


Fig. 20. Coefficient of determination (R^2) obtained by the ANFIS, ANN, and quadratic response-surface regression models for the north-, east-, south-, and west-facing façades.

is very high, confirming that the model also adequately reproduces the mean LGV patterns for the west-facing orientation.

The 2D projections for the south- and north-facing orientations, shown in Fig. 16 and Fig. 17, respectively, present more contrasting behaviors than those previously observed for the east- and west-facing orientations. For the south-facing orientation, the maps show a more intense and broader LGV response, with high values extending across the regions of higher DNI and cos(θ), confirming the greater weight of the direct component when the incidence geometry is favorable. This pattern is more marked than in the east- and west-facing orientations, where the response was similar between both façades but somewhat more balanced in its distribution. For the north-facing orientation, in contrast, the LGV range is clearly lower, and the response appears less dominated by the DNI-cos(θ) combination. The distribution shows a greater influence of DHI, consistent with an orientation where the diffuse component has greater relative weight. Unlike the east- and west-facing orientations, which present comparable patterns due to their geometric symmetry, the north- and south-facing orientations represent the two extremes of radiative behavior: Fig. 16 concentrates the highest values and Fig. 17 the lowest ones. In both cases, the similarity between the experimental and ANFIS maps confirms that the model adequately reproduces these differentiated patterns.

4.3. Statistical performance and independent evaluation of the ANFIS models

This Section presents the statistical results obtained with Eqs. (8)–(12). Table 3 and Table 4 show the performance of the ANFIS models for the four orientations, for both the training dataset and the independent test dataset. In training, the nRMSE values range from 12.2% to 16.4%, while in testing they remain between 12.1% and 15.4%, indicating consistent performance between the training and the independent test datasets. In addition, the nMAE values are lower than the nRMSE values in all cases, with values ranging from 7.3% to 9.5%, indicating that the mean absolute error remains relatively low. The nMBE is practically zero in training and very low in testing, with small deviations between −1.4% and 0.8%. This indicates that the models do not show any relevant systematic bias, although a slight underestimation is observed for the north-facing orientation in the test dataset. The R^2 and IA values are high for all orientations, especially for E, W, and S, with R^2 values close to or greater than 0.98 and IA values above 0.996 in most cases. The north-facing orientation shows the lowest fit, especially in testing, with $R^2 = 0.8964$ and IA = 0.9725, although these values still indicate adequate predictive capability considering the lower availability of the direct component and the greater influence of diffuse radiation on this façade. Overall, the results confirm that the ANFIS models reproduce global vertical illuminance accurately for the four orientations.

Fig. 18 summarizes the normalized performance metrics obtained for the ANFIS models in the four orientations, using 115,250 training records (year 2024) and 118,775 independent test records for the year 2025. The nRMSE values obtained for the test set remain within a narrow range, which indicates robust predictive performance considering the large size and variability of the dataset, including different sky conditions, solar geometries, and illuminance levels. In addition, the nMAE values are lower and the nMBE values are also close to zero, with only small positive or negative deviations depending on the orientation, indicating limited mean systematic bias. These results show that the proposed ANFIS models provide accurate and stable predictions of global vertical illuminance across all façade orientations. In view of the results obtained for the training and test data shown in Fig. 18, the reproducibility of the developed models was analyzed over five years prior to 2024, which were therefore not used in model fitting.

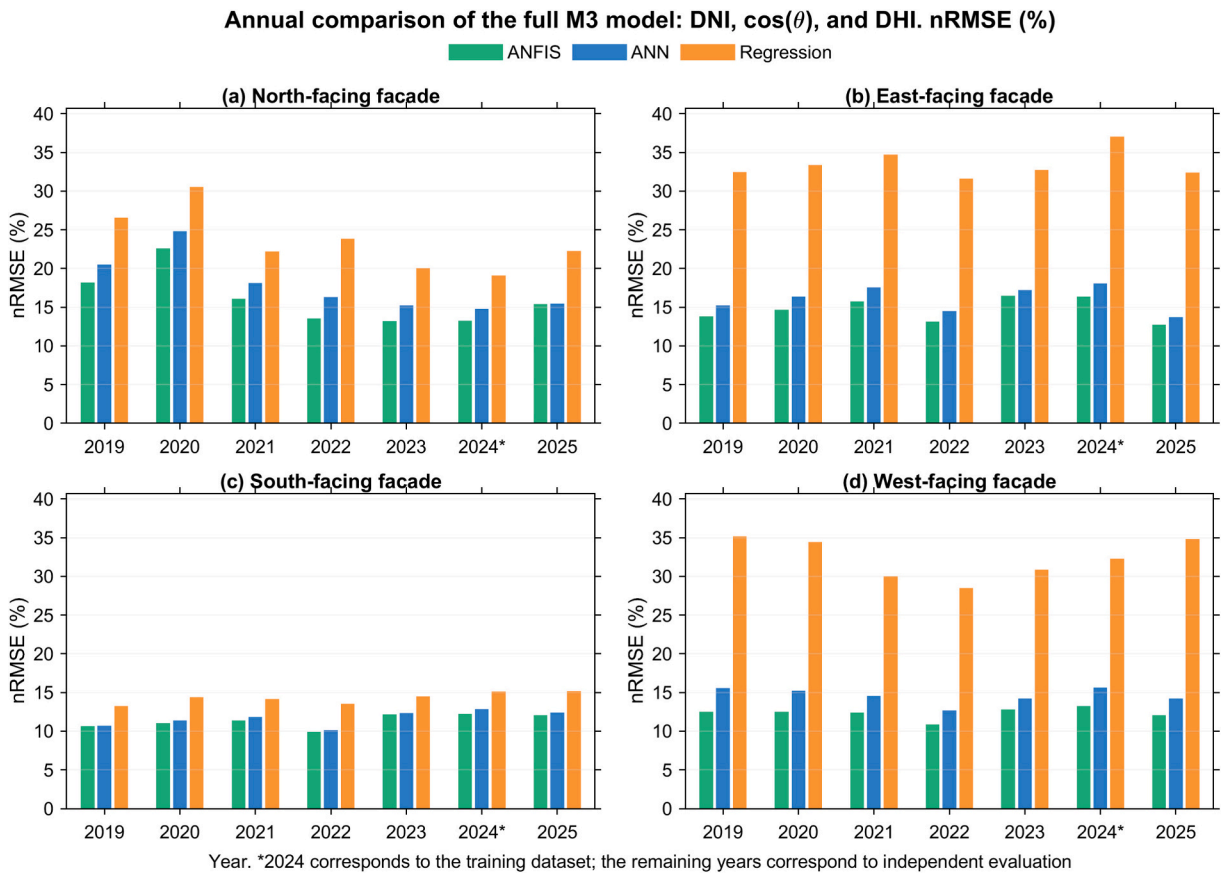


Fig. 21. nRMSE obtained by the ANFIS, ANN, and quadratic response-surface regression models for the north-, east-, south-, and west-facing façades.

As shown in Fig. 19, the ANFIS models exhibit overall stable behavior between 2019 and 2025, although only 2024 was used for model training. In the normalized error metrics, nRMSE and nMAE, the N orientation shows somewhat higher values, indicating that it is the most difficult orientation to reproduce. This is consistent with a greater dependence on diffuse and reflected radiation and on more variable sky conditions. The E, S, and W orientations show lower and more stable errors, with the S orientation generally among the best-performing cases. These results indicate that the proposed approach can estimate global vertical illuminance (LGV) with good accuracy using only basic radiometric and geometric variables, namely DNI, DHI, and cos(θ). This is especially relevant because it does not require measured global vertical irradiance values as input and facilitates its application to databases where only horizontal solar irradiance components are available. The consistent interannual performance, together with the high R^2 values and low normalized errors, indicates that the models consistently represent the empirical relationship among direct irradiance, diffuse irradiance, and solar geometry at the study site. Tables 3–9 show the results graphically represented in Fig. 19.

To complement the normalized error metrics, Table 10 reports the absolute RMSE and MAE values, expressed in lux, for the four façade orientations. Across the six independent evaluation years, RMSE ranged from 1086.1 to 2915.1 lx, whereas MAE ranged from 789.1 to 1798.8 lx. In the 2024 training year, RMSE ranged from 1032.2 to 2420.4 lx, while MAE ranged from 745.9 to 1494.2 lx.

4.4. Baseline comparison with regression and ANN models

Table 11 reports the arithmetic mean of the six annual values obtained for each performance metric during the independent evaluation period for the comparison using DNI, cos(θ), and DHI as predictors. Considering the 24 combinations formed by the four orientations and the six independent years, the mean nRMSE was 13.59% for ANFIS, 15.00% for ANN, and 25.90% for quadratic regression. The corresponding mean nMAE values were 8.67%, 10.16%, and 19.20%, respectively. As can be observed, ANFIS and ANN therefore provided substantially lower errors than the quadratic response-surface models. The differences between ANFIS and ANN were comparatively small. ANFIS produced lower nRMSE and nMAE values than ANN for all four orientations, although the difference was particularly small for the south-facing façade. Across all orientations and independent years, the mean differences between ANN and ANFIS were 1.42 percentage points in nRMSE and 1.50 percentage points in nMAE, with ANFIS providing the lower mean errors. These results indicate that the two nonlinear methods provide broadly comparable predictive performance when architectures of approximately equivalent complexity are used, although ANFIS yielded lower mean errors during independent evaluation. A similar behavior was observed for the models with fewer input variables.

Likewise, the results obtained for the 2024 training dataset are shown in Table 12. ANFIS and ANN again exhibited similar performance, with nRMSE values ranging from 12.22% to 16.38% for ANFIS and from 12.88% to 18.08% for ANN. As in the independent evaluation, ANFIS produced lower nRMSE and nMAE values than ANN for all four façades. The quadratic regression model showed substantially higher errors for the east-, west-, and north-facing façades, with nRMSE values of 37.03%, 32.31%, and 19.11%, respectively. Its performance was closer to that of the nonlinear models for the south-facing façade, although its nRMSE and nMAE remained higher. The training results reproduce the same relative behavior observed during independent evaluation: ANFIS and ANN provide comparable performance, whereas the quadratic response surface has insufficient flexibility to represent the relationship between DNI, DHI, cos(θ), and LGV, particularly for the east- and west-facing façades.

The results show a moderate predictive advantage of ANFIS over

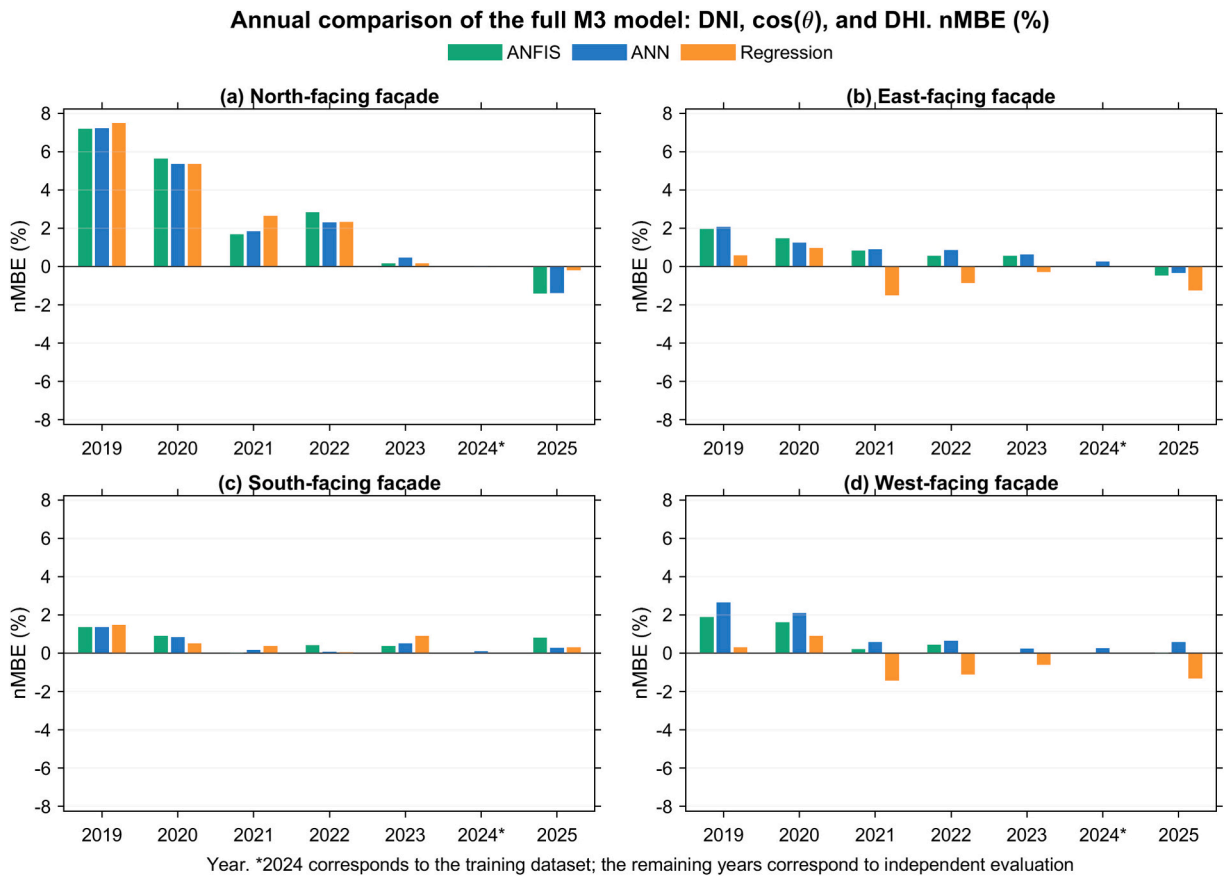


Fig. 22. nMBE obtained by the ANFIS, ANN, and quadratic response-surface regression models for the north-, east-, south-, and west-facing façades.

ANN. In addition, the relevance of ANFIS lies in combining predictive performance with a more interpretable neuro-fuzzy structure. In the M3 model, each input is represented by four partially overlapping Gaussian membership functions, producing 64 Sugeno rules associated with specific regions of the DNI-cos(θ)-DHI input space. This structure makes it possible to examine which rules are activated for a particular observation, their relative activation strengths, and the consequent values contributing to the final estimate.

Figs. 20–24 show the annual performance of the M3 models for the training year and the six independent evaluation years. ANFIS and ANN exhibit similar interannual patterns. In contrast, quadratic regression produces consistently higher nRMSE and nMAE values, particularly for the east- and west-facing façades. Its performance is comparatively better for the south-facing façade but remains below that of ANFIS and ANN. The similar relative behavior observed during training and independent evaluation indicates that the differences between the methods are not limited to a particular evaluation year.

As shown above, considering the mean values obtained over the six independent evaluation years, the nRMSE of the ANFIS model ranged from 11.21% to 16.50%, that of the ANN ranged from 11.41% to 18.50%, and that of quadratic regression ranged from 14.17% to 32.88%, depending on the orientation analyzed. The mean nMAE values ranged from 7.11% to 11.61% for ANFIS, from 7.79% to 13.17% for the ANN, and from 10.05% to 25.08% for quadratic regression.

Regarding published models that use an equivalent definition of relative RMSE, the best conventional model developed by Kong and Kim [20] obtained annual values of 24.79%, 22.68%, 15.97%, and 21.37% for the north-, east-, south-, and west-facing orientations, respectively. Aghimien and Li [18] reported monthly values ranging from 10.6% to 39.9%, depending on the month and orientation. The ANFIS models generally yielded lower errors than these conventional models.

In contrast, the machine-learning models evaluated by Li and Aghimien [25] using independent data obtained values ranging from 7.7% to 16.8%. The results of the present study are therefore of the same order of magnitude, although they are not lower for all orientations. It should also be noted that the models developed by Li and Aghimien [25] use measured vertical irradiance, whereas the proposed methodology estimates LGV directly from DNI, DHI, and incidence geometry.

According to the accuracy classification adopted by Li and Aghimien [25], 23 of the 24 results corresponding to the four orientations and the six independent years can be classified as good or excellent. The only exception is the north-facing façade in 2020, whose nRMSE of 22.60% is classified as acceptable. Therefore, the accuracy achieved in the present study can be considered adequate for estimating LGV at the study site when direct measurements are unavailable, particularly for the east-, south-, and west-facing orientations.

4.5. Error analysis under different sky, seasonal, and solar-geometry conditions

To examine the robustness of the three-input ANFIS models in greater detail, an error analysis was performed using exclusively the six independent evaluation years, 2019–2023 and 2025. The same all-sky models developed using the 2024 data were retained without retraining and analyzed according to sky condition, season, solar altitude, and cos(θ). This makes it possible to examine the extent to which the relationships learned from the 2024 data are maintained under different sky conditions, seasons, and solar-geometry configurations.

Sky conditions were classified using the eight intervals of the Perez et al. [31] sky-clearness index, from P1 ($1 \leq \varepsilon \leq 1.065$), corresponding to the most overcast conditions, to P8 ($\varepsilon \geq 6.2$), associated with the clearest conditions. The seasonal analysis considered winter, spring,

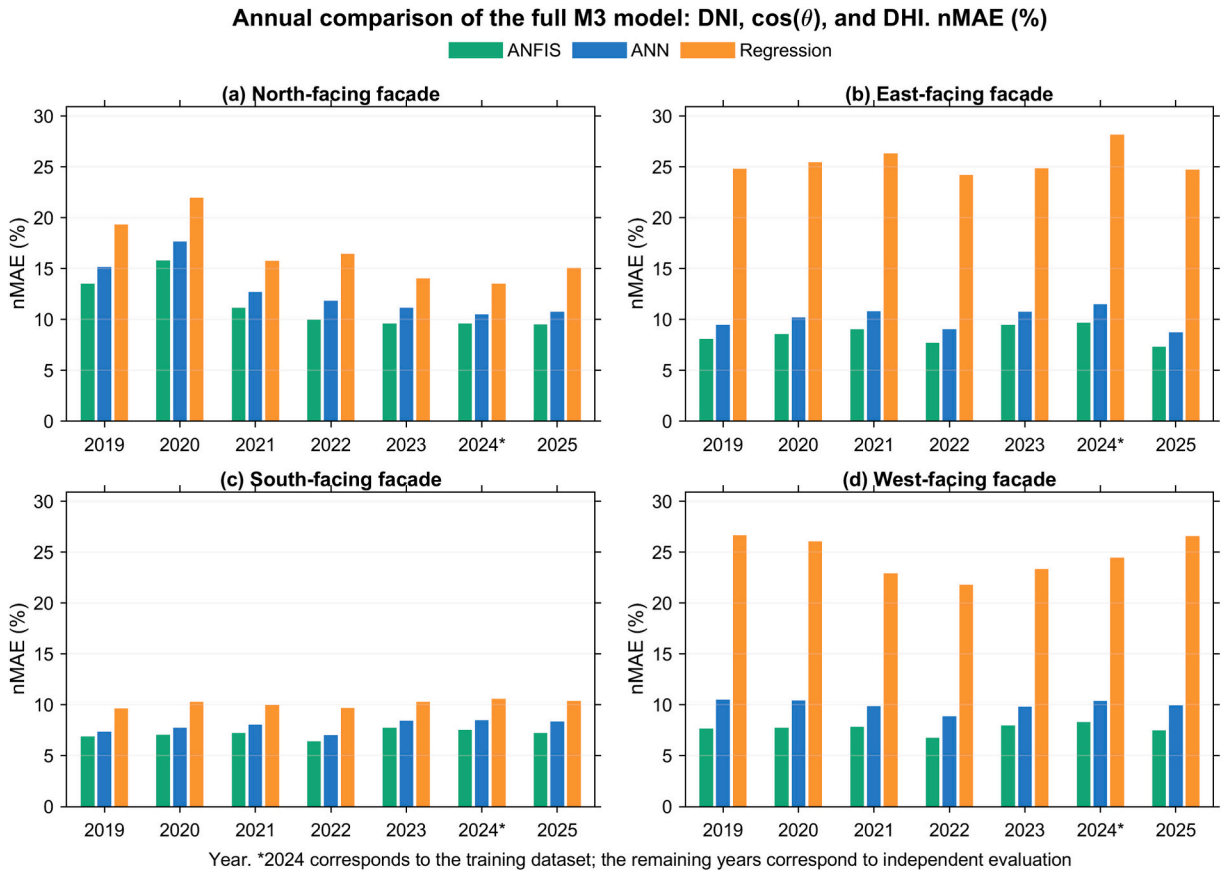


Fig. 23. nMAE obtained by the ANFIS, ANN, and quadratic response-surface regression models for the north-, east-, south-, and west-facing façades.

summer, and fall. Solar geometry was evaluated using four solar-altitude intervals and four cos(θ) intervals, together with a joint analysis of both variables. For each orientation and subset, nRMSE and nMBE were calculated.

Analysis of Fig. 25 shows a clear dependence of the error on the Perez sky-clearness interval. For all four orientations, the highest nRMSE values occur in the first intervals, corresponding to lower-clearness conditions, and progressively decrease toward P8. The maximum value is generally obtained in P2, reaching approximately 24% for the north-facing façade, 31% for the east-facing façade, 26% for the south-facing façade, and 23% for the west-facing façade. From P3 onward, the error decreases steadily, particularly for the east-, south-, and west-facing façades, for which nRMSE reaches values close to 6%, 5%, and 6%, respectively, in P8. For the north-facing façade, the reduction is less pronounced, and nRMSE remains around 13% in the highest-clearness intervals.

The behavior of nMBE is more dependent on orientation. For the east-, south-, and west-facing façades, a marked underestimation is observed in P2, with values ranging approximately from −14% to −17%. Its magnitude decreases in P3 and changes to slight overestimation from P4 onward. In the P4-P8 intervals, the bias generally remains close to zero. The north-facing façade shows small positive biases in the first intervals, which progressively increase toward higher-clearness conditions and reach approximately 6% in P8. The results show a general improvement in accuracy as sky clearness increases, although the transition between the first intervals is not strictly monotonic and the bias behavior depends on orientation.

The seasonal analysis shown in Fig. 26 indicates that the highest errors occur in winter for all four orientations. This effect is particularly pronounced for the north-facing façade, where nRMSE reaches approximately 32%, compared with values of about 12% to 17% during the rest of the year. For the east- and west-facing façades, winter nRMSE is around 20%, whereas in spring, summer, and fall it decreases to approximately 10% to 15%. The south-facing façade shows the most stable behavior and the lowest seasonal errors, with an nRMSE close to 14% in winter and below 11% during the other seasons.

The nMBE results confirm that the deterioration in winter is not due solely to greater dispersion, but also to systematic overestimation. The positive bias reaches approximately 10% for the north-facing façade, 5% for the east-facing façade, 3% for the south-facing façade, and 6% for the west-facing façade. In spring, the bias decreases markedly, while in summer it becomes slightly negative for all orientations. During fall, nMBE remains close to zero, except for the north-facing façade, where moderate overestimation is still observed.

The joint analysis of solar altitude and incidence geometry shown in Fig. 27 indicates that the highest errors generally occur within the solar-altitude interval from 5° to 15°. This effect is particularly pronounced for the north-facing façade, where nRMSE reaches approximately 39% when the Sun is clearly behind the façade, with $-1 \leq \cos(\theta) < -0.5$. Increased errors at low solar altitudes are also observed for the east-, south-, and west-facing façades, although the most unfavorable combinations depend on orientation. For the south-facing façade, for example, nRMSE increases to approximately 28% under highly positive incidence conditions, whereas the maximum values for the east- and west-facing façades are approximately 23% and 19%, respectively.

As solar altitude increases, the errors decrease for most geometric combinations. At solar altitudes above 30°, nRMSE values generally remain between approximately 6% and 15%, except under some unfavorable conditions for the north-facing façade. This indicates that the model reproduces LGV more accurately when the solar position is higher and the relationship among direct irradiance, diffuse irradiance, and incidence geometry is better defined.

The nMBE results show a similar trend. The largest positive biases occur mainly at low solar altitudes, reaching approximately 16% for the

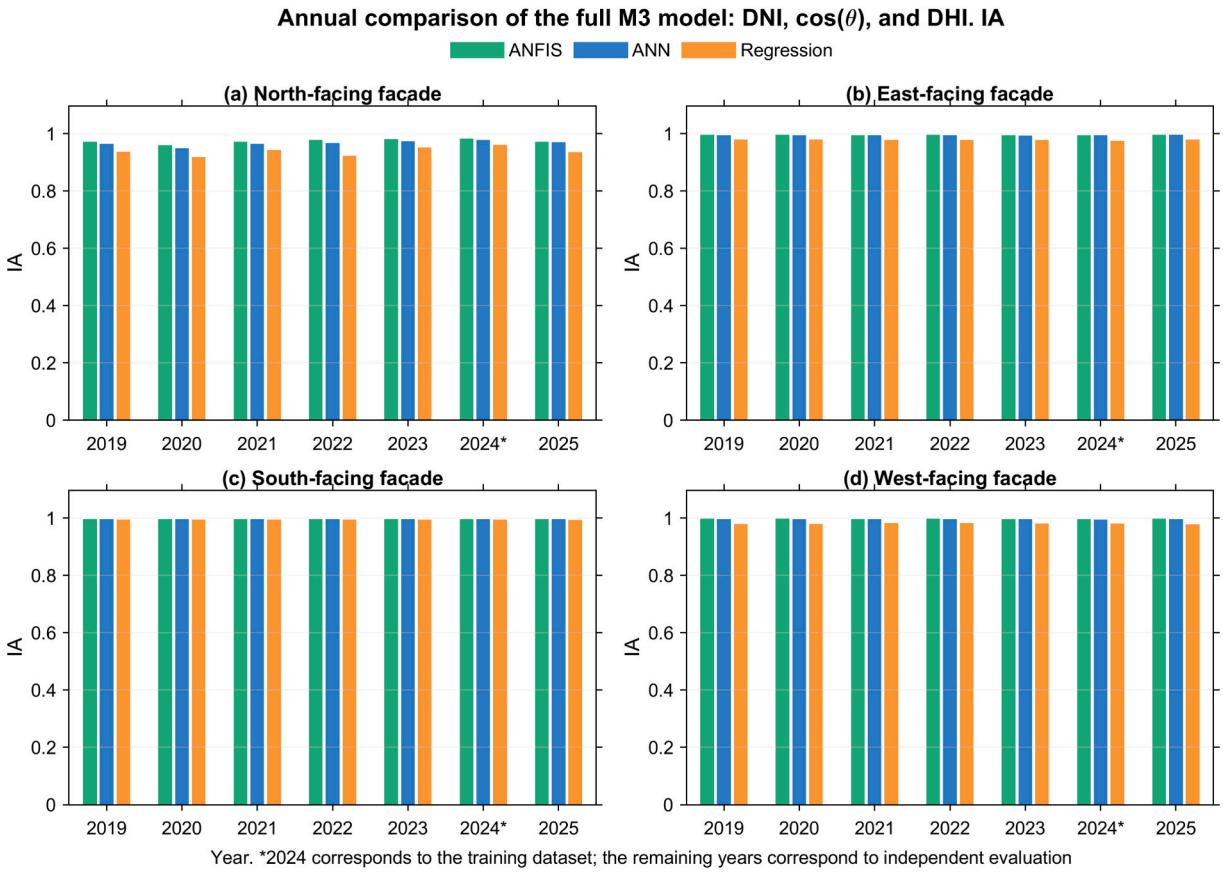


Fig. 24. Index of agreement (IA) obtained by the ANFIS, ANN, and quadratic response-surface regression models for the north-, east-, south-, and west-facing façades.

north-facing façade and values close to 10% to 14% for some combinations corresponding to the east-, south-, and west-facing façades. At medium and high solar altitudes, the bias generally remains close to zero, although some moderate positive or negative deviations are observed depending on orientation and cos(θ). Cells marked as NA correspond to geometric combinations with no valid records, as a consequence of the available solar geometry and the filtering criteria applied.

The separate analysis of solar altitude shown in Fig. 28 confirms the trend observed in the joint geometric analysis. For all four orientations, the highest nRMSE and nMBE values occur at solar altitudes between 5° and 15°, with a particularly pronounced effect for the east- and south-facing façades. As solar altitude increases, both error and bias generally decrease, reaching their lowest values at solar altitudes above 30°. The west-facing façade shows a slight deviation from this trend at solar altitudes above 45°, although its errors remain clearly lower than those obtained under low-sun conditions.

The separate analysis of cos(θ) shows that the effect of solar incidence depends on orientation. As shown in Fig. 29, the north-facing façade exhibits the highest error when the Sun is clearly behind the surface, whereas for the east- and west-facing façades, nRMSE tends to decrease as the incidence changes from negative to positive. The south-facing façade likewise shows lower errors for positive values of cos(θ). The nMBE generally remains close to zero, except under some unfavorable incidence conditions, particularly for the north-facing façade.

The highest errors occur under overcast skies, during winter, and at solar altitudes between 5° and 15°, particularly for the north-facing façade. The geometric analysis confirms that the influence of cos(θ) depends on orientation and that combinations of low solar altitude and unfavorable incidence represent the most demanding conditions. This behavior may be related to the greater relative contribution of the diffuse and reflected components and to the greater sensitivity of vertical illuminance to small changes in solar geometry. In addition, the lower mean LGV values in some of these subsets may increase the normalized errors. Under the remaining conditions, nMBE generally remains close to zero, indicating limited systematic bias.

Therefore, the results obtained for the independent years (2019–2023 and 2025), which were not used during model training, indicate consistent temporal performance of the developed models at the study site. However, spatial generalization cannot be established from the present results because the developed models need to be validated using independent datasets from other measurement sites to assess their transferability under different environmental conditions.

5. Conclusions

This study developed four ANFIS models to estimate global vertical illuminance (LGV) on north-, east-, south-, and west-facing façades under all-sky conditions. The models use three radiometric and geometric predictors that can be measured or calculated from data commonly available at radiometric stations: direct normal irradiance, diffuse horizontal irradiance, and the façade-specific cosine of the incidence angle. The main contribution of the proposed methodology is the direct estimation of LGV without requiring measured vertical irradiance, explicit sky classification, or an intermediate luminous-efficacy calculation.

The models were trained exclusively with 115,250 records from 2024 and evaluated with 750,294 records from six independent years, corresponding to 2019–2023 and 2025. For the training dataset, nRMSE ranged from 12.22% to 16.38% and nMAE from 7.54% to 9.70%. Across the six independent years, nRMSE ranged from 9.91% to 22.60%, nMAE from 6.44% to 15.83%, R^2 from 0.855 to 0.991, and IA from 0.960 to 0.998. The east-, south-, and west-facing models maintained nRMSE values of 16.50% or lower, whereas the north-facing model presented

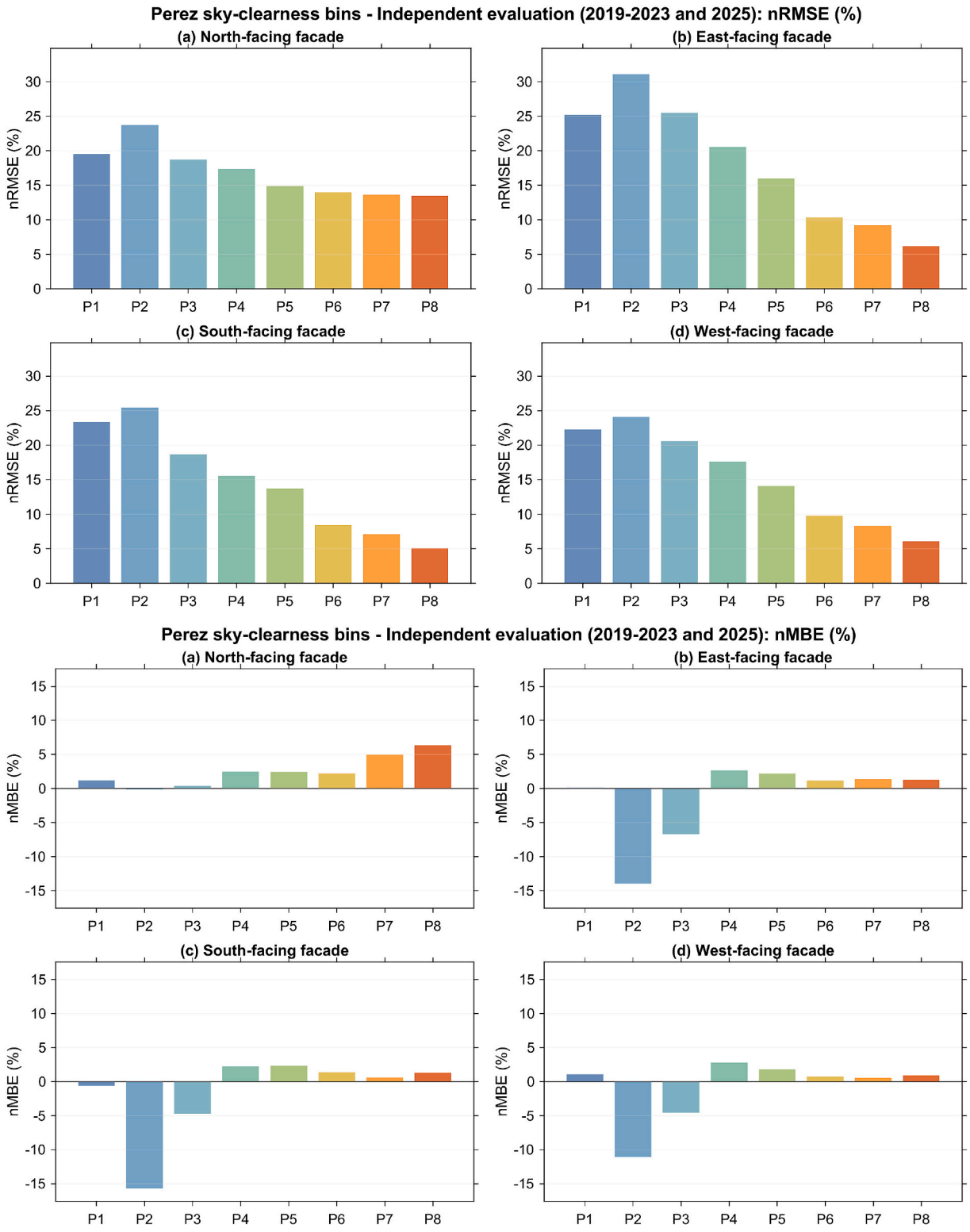


Fig. 25. nRMSE and nMBE of the M3 ANFIS models for the eight sky-clearness intervals defined by Perez et al. [31] during the six independent evaluation years.

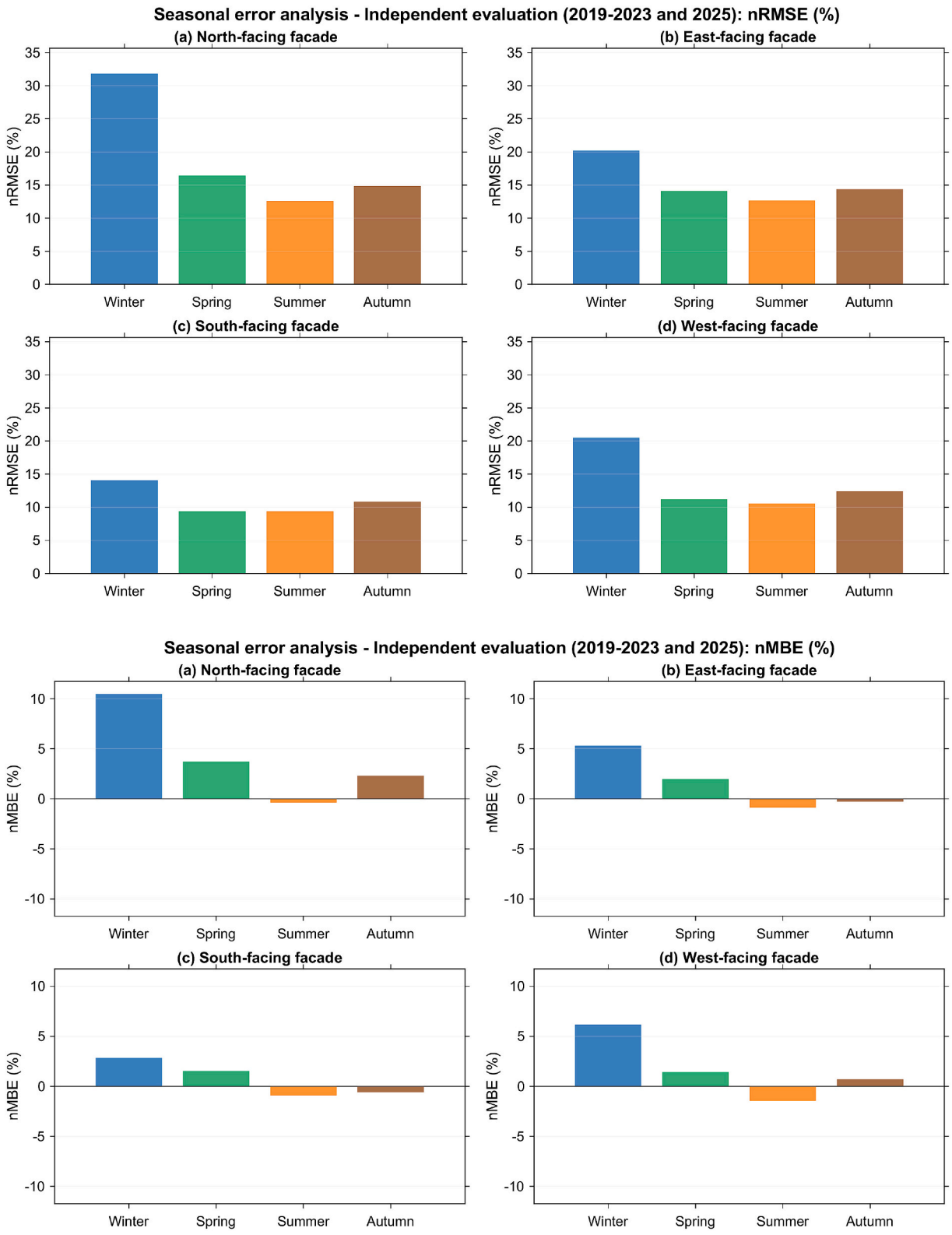


Fig. 26. Seasonal nRMSE and nMBE of the M3 ANFIS models during the six independent evaluation years.

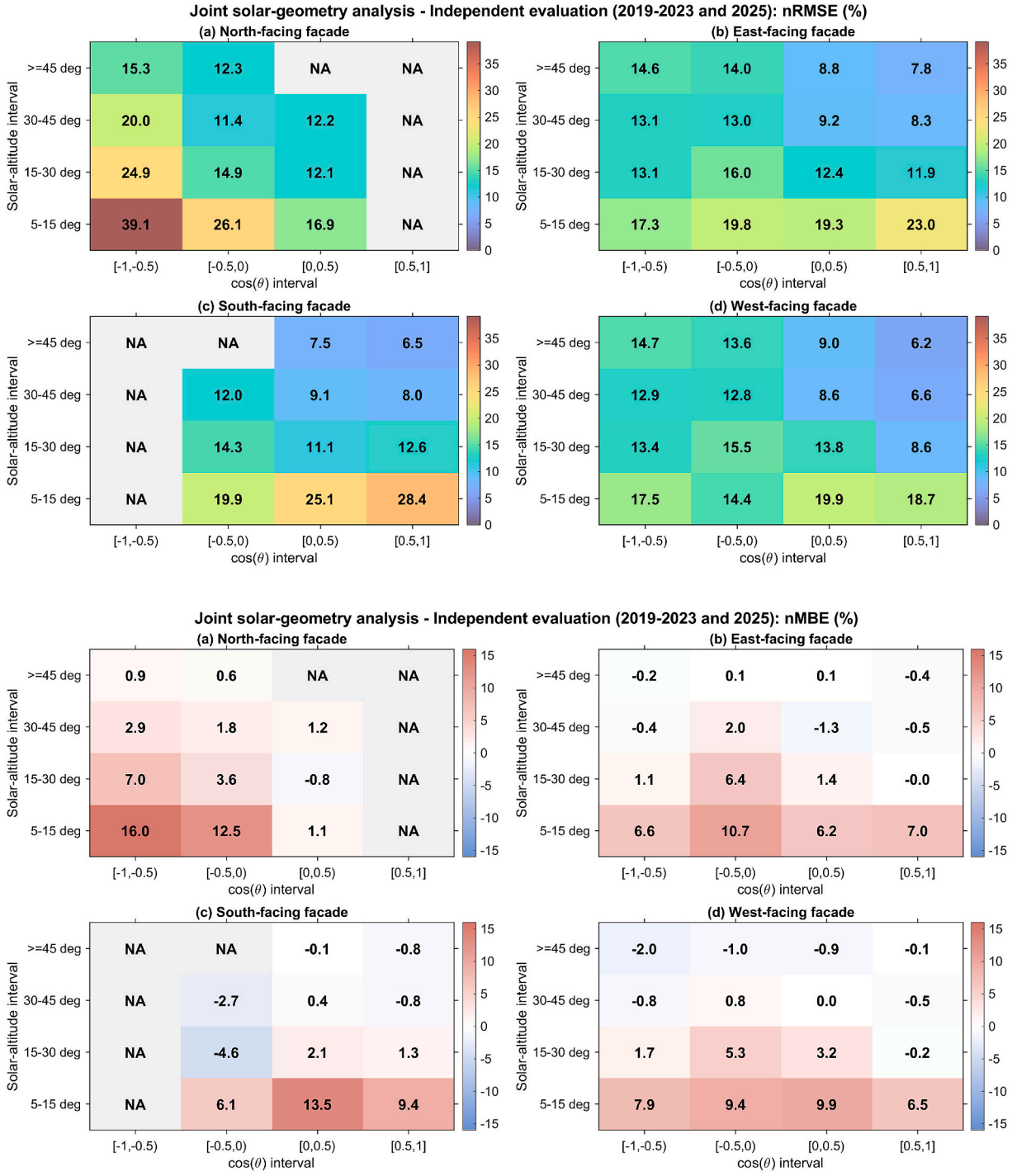


Fig. 27. nRMSE and nMBE of the M3 ANFIS models as functions of solar altitude and cos(θ) during the six independent evaluation years.

the highest errors, particularly in 2020. This orientation was therefore the most difficult to reproduce, which is consistent with its lower direct contribution and greater relative dependence on diffuse radiation.

The contribution of DHI was quantified by comparing the reduced M2 models, based on DNI and cos(θ), with the complete M3 models, based on DNI, cos(θ), and DHI. For the combined six-year independent dataset, including DHI reduced nRMSE by 46.4% to 59.5% and nMAE by 56.5% to 64.7%, depending on façade orientation. Both errors decreased in all 24 orientation-year combinations, with the largest relative improvement obtained for the north-facing façade. These results confirm that DHI provides predictive information that cannot be represented using only DNI and incidence geometry and support its inclusion in the proposed models.

The baseline comparison showed that ANFIS and ANN achieved comparable predictive accuracy, whereas quadratic regression produced substantially higher errors, particularly for the east- and west-facing façades. The condition-based analysis showed that the largest errors occurred under low sky-clearness conditions, during winter, and at solar altitudes between 5° and 15°, especially for the north-facing façade. Under the remaining conditions, the models generally maintained limited systematic bias.

The results support the use of the proposed ANFIS models to estimate

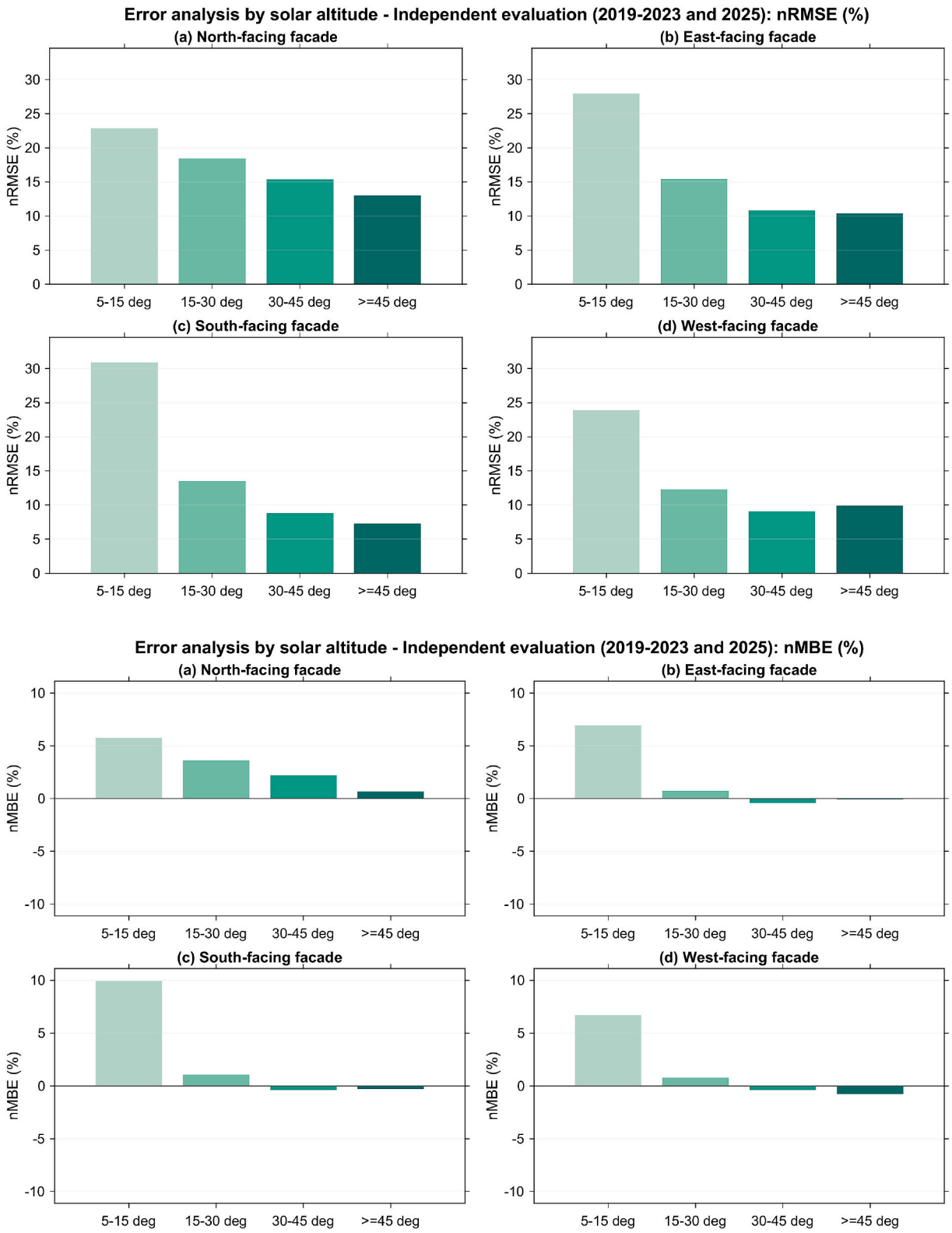


Fig. 28. nRMSE and nMBE of the M3 ANFIS models for different solar-altitude intervals during the six independent evaluation years.

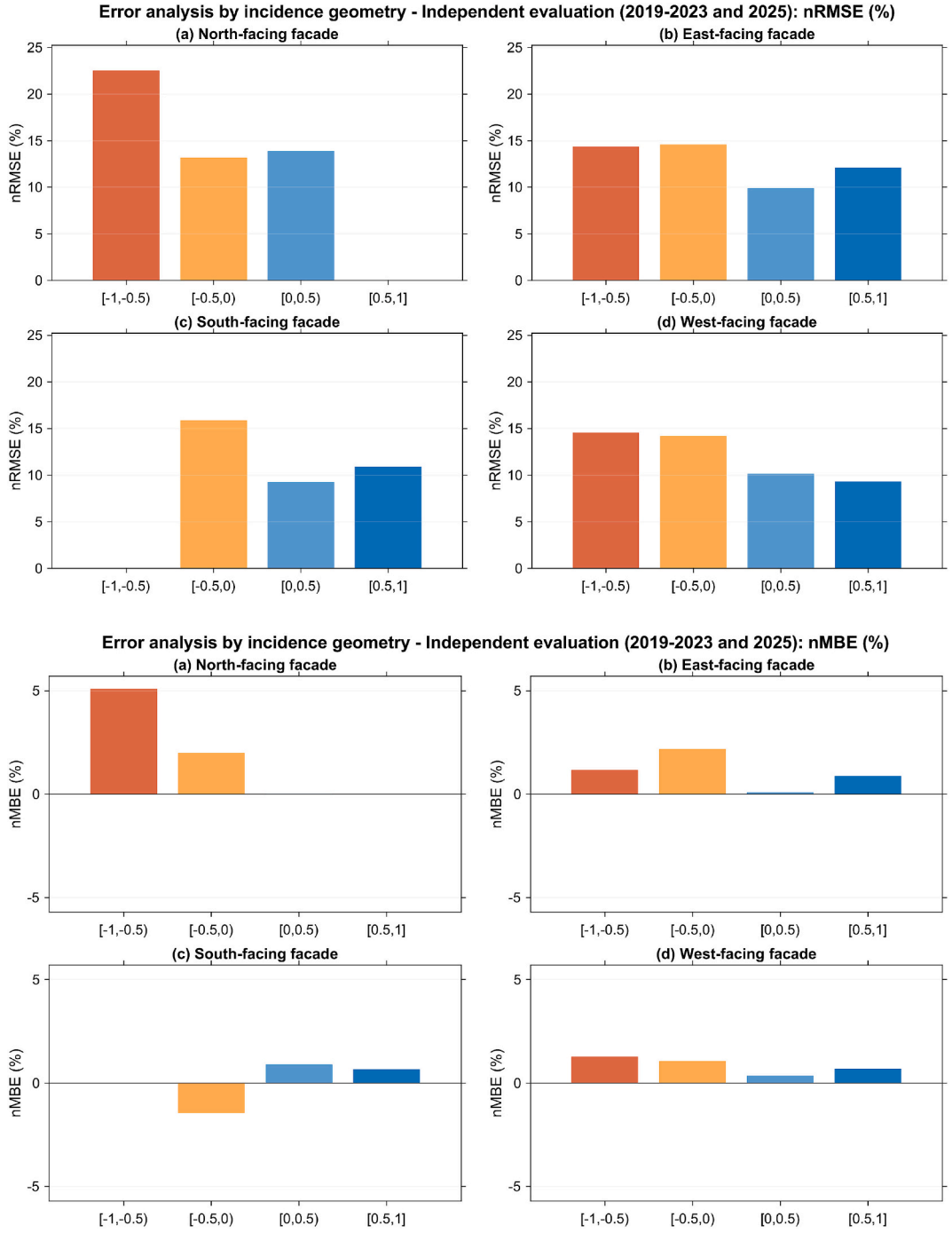


Fig. 29. nRMSE and nMBE of the M3 ANFIS models for different cos(θ) intervals during the six independent evaluation years.

LGV at the study site when direct LGV measurements are unavailable and demonstrate consistent performance over the evaluated years.

Their transferability to other locations cannot be inferred from the present results and should be assessed in future work using independent measurements from additional sites.

CRediT authorship contribution statement

M.I. Dieste-Velasco: Writing – review & editing, Writing – original draft, Visualization, Validation, Software, Methodology, Formal analysis, Conceptualization.

Funding

Open access funding provided by Universidad de Burgos.

Declaration of competing interest

The author declares no known competing financial interests or personal relationships that could have appeared to influence the work reported in this paper.

Acknowledgements

The author gratefully acknowledges Dr. Dominique Dumortier of

ENTPE (France) for providing access to the experimental data used in this study.

Data availability

Access to the experimental data supporting the findings of this study was provided by Dr. Dominique Dumortier from ENTPE (France).

References

[1] A. Ahmad, A. Kumar, O. Prakash, A. Aman, Daylight availability assessment and the application of energy simulation software – a literature review, Mater. Sci. Energy Technol. 3 (2020) 679–689, https://doi.org/10.1016/j.mset.2020.07.002.

[2] M. Gholami Rostam, A. Abbasi, Enhancing building energy efficiency through a climate adaptive design: considering upcoming extreme climate conditions, J. Clean. Prod. 450 (2024) 141747, https://doi.org/10.1016/j.jclepro.2024.141747.

[3] E.I. Aghimien, D.H.W. Li, W. Chen, E.K.W. Tsang, Daylight luminous efficacy: an overview, Sol. Energy. 228 (2021) 706–724, https://doi.org/10.1016/j.solener.2021.05.018.

[4] M. Dastoum, C. Sanchez Guevara, B. Arranz, Efficient daylighting and thermal performance through tessellation of geometric patterns in building façade: a systematic review, Energy Sustain. Dev. 83 (2024) 101563, https://doi.org/10.1016/j.esd.2024.101563.

[5] S.M. Hosseini, S. Heidari, S. Attia, J. Wang, G. Triantafyllidis, Biomimetic kinetic façade as a real-time daylight control: complex form versus simple form with proper kinetic behavior, Smart Sustain. Built Environ. (2024) 472–507, https://doi.org/10.1108/SASBE-03-2024-0090.

[6] N. Eisazadeh, F. De Troyer, K. Allacker, Environmental performance of patient rooms using an integrated approach considering operational energy, daylight and comfort analysis, Smart Sustain. Built Environ. 14 (2025) 1117–1142, https://doi.org/10.1108/SASBE-07-2023-0173.

[7] M. Wang, P. Fang, B. Lv, D. Yang, X. Zheng, H. Gao, A novel multi-zone uniform lighting control strategy for buildings based on SSA and ELM, Build. Simul. 18 (2025) 2899–2921, https://doi.org/10.1007/s12273-025-1343-6.

[8] H.G. Castellanos, Y. Aryanfar, A.N. Sadabad, A. Keçebaş, M. Youssef, F. Akhgarzarandy, M. Farzinfar, S.M. Ghasemlou, A. Ghazy, K. Kaaniche, Integrating solar energy in urban development: strategies for sustainable and smart cities, Int. Trans. Electr. Energy Syst. 2025 (2025). doi:https://doi.org/10.1155/etep/6096036.

[9] L. Hong, X. Zhang, J. Du, A benchmarking analysis of sunlight and daylight availability in a highly dense urban area in southern China, Energ. Buildings 323 (2024), https://doi.org/10.1016/j.enbuild.2024.114847.

[10] S.G. Colaco, C.P. Kurian, V.I. George, A.M. Colaco, Model based evaluation of exterior daylight illuminance distribution, Build. Simul. 2 (2009) 85–94, https://doi.org/10.1007/s12273-009-9113-4.

[11] D.H.W. Li, J.C. Lam, Predicting vertical luminous efficacy using horizontal solar data, Light. Res. Technol. 33 (2001) 25–42, https://doi.org/10.1177/136578280103300107.

[12] M. Manni, J.K. Thorning, S. Jouttijärvi, K. Miettunen, M. Di Sabatino, G. Lobaccaro, Horizontal-to-tilt irradiance conversion for high-latitude regions: a review and meta-analysis, Front. Built Environ. 9 (2023), https://doi.org/10.3389/fbuil.2023.1245223.

[13] A. Mahdavi, S. Dervishi, A comparison of luminous efficacy models based on data from Vienna, Austria, Build. Simul. 4 (2011) 183–188, https://doi.org/10.1007/s12273-011-0021-z.

[14] M.S. Mayhoub, D.J. Carter, A model to estimate direct luminous efficacy based on satellite data, Sol. Energy. 85 (2011) 234–248, https://doi.org/10.1016/j.solener.2010.12.008.

[15] A.S. Azad, D. Rakshit, K.N. Patil, Model development and evaluation of global and diffuse luminous efficacy for humid sub-tropical region, Renew. Energy 119 (2018) 375–387, https://doi.org/10.1016/j.renene.2017.12.004.

[16] H.J. Kong, J.T. Kim, Modeling luminous efficacy of daylight for Yongin, South Korea, Energ. Buildings 62 (2013) 550–558, https://doi.org/10.1016/j.enbuild.2013.03.037.

[17] D.H.W. Li, T.N.T. Lam, K.L. Cheung, H.L. Tang, An analysis of luminous efficacies under the CIE standard skies, Renew. Energy 33 (2008) 2357–2365, https://doi.org/10.1016/j.renene.2008.02.004.

[18] E.I. Aghimien, D.H.W. Li, Application of luminous efficacies for daylight illuminance data generation in subtropical Hong Kong, Smart Sustain. Built Environ. 11 (2022) 271–293, https://doi.org/10.1108/SASBE-08-2021-0146.

[19] A. De Rosa, V. Ferraro, D. Kaliakatsos, V. Marinelli, Calculating diffuse illuminance on vertical surfaces in different sky conditions, Energy 33 (2008) 1703–1710, https://doi.org/10.1016/j.energy.2008.05.009.

[20] H.J. Kong, J.T. Kim, Evaluation of global vertical illuminance and irradiance models against data from Yongin, South Korea, Energ. Buildings 91 (2015) 139–147, https://doi.org/10.1016/j.enbuild.2015.01.025.

[21] Y. Yang, L. Gu, Application of dynamic lighting based on fuzzy neural network in traditional art modelling, Int. J. Fuzzy Syst. (2025), https://doi.org/10.1007/s40815-025-02043-8.

[22] Z. Ye, C. Li, Evaluation and optimization of light environments for typical art and design classrooms in university buildings, J. Build. Pathol. Rehabil. 11 (2026) 37, https://doi.org/10.1007/s41024-025-00713-6.

[23] S. Jović, O. Aničić, M. Marsenić, B. Nedić, Solar radiation analyzing by neuro-fuzzy approach, Energ. Buildings 129 (2016) 261–263, https://doi.org/10.1016/j.enbuild.2016.08.020.

[24] M. Şahin, Y. Oluz, F. Büyüktümtürk, ANN-based estimation of time-dependent energy loss in lighting systems, Energy Build. 116 (2016) 455–467, https://doi.org/10.1016/j.enbuild.2016.01.027.

[25] D.H.W. Li, E.I. Aghimien, Predicting vertical daylight illuminance data from measured solar irradiance: a machine learning-based luminous efficacy approach, J. Sol. Energy Eng. Trans. ASME 145 (2023) 1–16, https://doi.org/10.1115/1.4055915.

[26] D.H.W. Li, E.I. Aghimien, E.K.W. Tsang, Application of artificial neural networks in horizontal luminous efficacy modeling, Renew. Energy 197 (2022) 864–878, https://doi.org/10.1016/j.renene.2022.08.016.

[27] The MathWorks Inc., in: The MathWorks, Inc. (Ed.), Fuzzy Logic Toolbox™ User's Guide, 2022. © Copyright 1995–2022 by.

[28] CIE, 108-1994,. guide to recommended practice of daylight measurement, technical report, Commun. Int. l'Eclairage, 1994.

[29] T. Zhang, P.W. Stackhouse, B. Macpherson, J. Colleen Mikovitz, A CERES-based dataset of hourly DNI, DHI and global tilted irradiance (GTI) on equatorward tilted surfaces: derivation and comparison with the ground-based BSRN data, Sol. Energy. 274 (2024) 112538, https://doi.org/10.1016/j.solener.2024.112538.

[30] C.A. Gueymard, A reevaluation of the solar constant based on a 42-year total solar irradiance time series and a reconciliation of spaceborne observations, Sol. Energy 168 (2018) 2–9, https://doi.org/10.1016/j.solener.2018.04.001.

[31] R. Perez, P. Ineichen, R. Seals, J. Michalsky, R. Stewart, Modeling daylight availability and irradiance components from direct and global irradiance, Sol. Energy. 44 (1990) 271–289, https://doi.org/10.1016/0038-092X(90)90055-H.

[32] H.T. Nguyen, M. Sugeno (Eds.), Fuzzy Systems, Springer US, Boston, MA, 1998, https://doi.org/10.1007/978-1-4615-5505-6.

[33] C.J. Willmott, On the validation of models, Phys. Geogr. 2 (1981) 184–194, https://doi.org/10.1080/02723646.1981.10642213.